### nature catalysis

**Article** 

https://doi.org/10.1038/s41929-025-01416-4

# Efficient and scalable upcycling of oceanic carbon sources into bioplastic monomers

Received: 23 August 2024

Accepted: 19 August 2025

Published online: 6 October 2025



Chengbo Li <sup>17</sup>, Mingming Guo<sup>2,3,7</sup>, Bo Yang<sup>4</sup>, Yuan Ji<sup>1</sup>, Jing Zhang<sup>5</sup>, Liujiang Zhou<sup>5,6</sup>, Chunxiao Liu <sup>1</sup>, Haoyuan Wang <sup>1</sup>, Jiawei Li <sup>1</sup>, Weiqing Xue<sup>1</sup>, Xinyan Zhang<sup>1</sup>, Hongliang Zeng<sup>1</sup>, Yanjiang Wang<sup>1</sup>, Donghao Zhao<sup>1</sup>, Kexin Zhong<sup>1</sup>, Shanshan Pi<sup>2</sup>, Minzhe Hei<sup>2</sup>, Xu Li <sup>1</sup>, Qiu Jiang <sup>1</sup>, Tingting Zheng <sup>1</sup>, Xiang Gao <sup>2</sup> & Chuan Xia <sup>1,6</sup> ✓

Renewable electricity-driven capture and conversion of oceanic dissolved inorganic carbon into value-added chemicals offers a sustainable route towards negative carbon emissions and a circular carbon economy. Here we present an artificial ocean carbon recycling system that captures and converts oceanic carbon sources into biochemicals through a decoupled electro-biocatalytic hybrid process. The system captures  $CO_2$  from natural seawater under very dilute yet realistic dissolved inorganic carbon conditions (2.16 mM) with high capture efficiency (>70%), low energy consumption (3 kWh kg $CO_2^{-1}$ ) and long stability (536 h). Techno-economic analysis revealed a competitive cost of capture (US\$229.9 t $CO_2^{-1}$ ). Using a highly efficient and stable bismuth-based electrocatalyst,  $CO_2$  was further converted into pure formic acid (800 mA cm $^{-2}$  at  $^{-1}$ .37 V) and subsequently transformed by engineered *Vibrio natriegens* into succinic acid (1.37 g l $^{-1}$ ). Therefore, our electro-bioconversion system represents a solution to sustainable biochemical synthesis using the ocean carbon sink as a resource.

The escalating costs and impacts of  $\mathrm{CO_2}$  emissions call for a radical shift in the production paradigm that balances economic feasibility and environmental friendliness. One such paradigm is the circular carbon economy, which targets the reduction, reuse, recycling and removal of  $\mathrm{CO_2}$  from both natural and anthropogenic sources within the carbon cycle. By responsibly tapping into natural carbon resources, we can create a closed-loop system in which carbon is both captured and repurposed, reducing the environmental impact of industries while facilitating the restoration and preservation of ecosystems.

As Earth's largest carbon reservoir, the ocean absorbs a substantial fraction (-26%) of anthropogenic  $CO_2$  emissions<sup>1,2</sup>. The uptake of excess  $CO_2$  by the ocean increases the partial pressure of  $CO_2$ , which

accumulates as dissolved inorganic carbon (DIC) in seawater and consists of free  $CO_2$  and bicarbonate ( $HCO_3^{-}$ ) and carbonate ( $CO_3^{2-}$ ) ions<sup>3</sup>. Consequently, the carbon content of the ocean is around 140 times greater than that of the atmosphere on a weight per volume basis<sup>3–7</sup>. This underscores the pivotal role of the ocean in carbon sequestration. Among natural sequestration mechanisms, biological carbon fixation by marine organisms, particularly phytoplankton via photosynthesis, constitutes a key pathway for  $CO_2$  capture and long-term storage within oceanic carbon sinks<sup>8–10</sup>. However, the rapid increase in atmospheric  $CO_2$  is disrupting the equilibrium between carbon emissions and biological carbon fixation, leading to ocean acidification that impairs marine ecosystems<sup>11,12</sup>. Moreover, ocean–atmosphere interactions

<sup>1</sup>School of Materials and Energy, University of Electronic Science and Technology of China, Chengdu, People's Republic of China. <sup>2</sup>State Key Laboratory of Quantitative Synthetic Biology, Shenzhen Institute of Synthetic Biology, Shenzhen Institutes of Advanced Technology, Chinese Academy of Sciences, Shenzhen, People's Republic of China. <sup>3</sup>University of Chinese Academy of Sciences, Beijing, People's Republic of China. <sup>4</sup>State Key Laboratory of Coordination Chemistry, School of Chemistry and Chemical Engineering, Nanjing University, Nanjing, People's Republic of China. <sup>5</sup>School of Physics, University of Electronic Science and Technology of China, Chengdu, People's Republic of China. <sup>6</sup>Yangtze Delta Region Institute (Huzhou), University of Electronic Science and Technology of China, Huzhou, Zhejiang, People's Republic of China. <sup>7</sup>These authors contributed equally: Chengbo Li, Mingming Guo. ⊠e-mail: gaoxiang@siat.ac.cn; chuan.xia@uestc.edu.cn

introduce the risk of a rebound effect, whereby previously sequestered oceanic  $\mathrm{CO}_2$  may potentially be re-released into the atmosphere under declining atmospheric  $\mathrm{CO}_2$  concentrations  $^{13}$ . Given the limited capacity and inherent vulnerability of natural biological carbon sinks to environmental perturbations, it is essential to engineer artificial ocean carbon sink systems. Such engineered systems should incorporate purposeful carbon valorization strategies by coupling efficient carbon capture with subsequent utilization processes. This strategy holds the potential to facilitate the sustainable use of the ocean carbon sink and supports environmentally responsible growth of the marine economy.

Electrochemical direct ocean capture (eDOC) has emerged as a sustainable solution for capturing CO<sub>2</sub> from the ocean and represents the crucial first step in oceanic CO<sub>2</sub> upcycling. In general, well-known direct air capture systems involve the sorption of very dilute CO<sub>2</sub> from the air, followed by the input of energy to desorb CO<sub>2</sub> into a concentrated stream. However, the naturally occurring ocean-atmosphere equilibrium removes the need for the energy-intensive CO<sub>2</sub> sorption step for eDOC technology, resulting primarily in capital and operation cost savings<sup>14</sup>. Current eDOC technology uses a bipolar membrane electrodialysis (BPMED) system to acidify and basify seawater<sup>15–17</sup>. The acidic stream produces CO<sub>2</sub> gas that can be collected and purified. Concurrently, the alkalization process restores the acidified seawater to its original pH, allowing it to be safely returned to the ocean where it serves again as a natural absorbent for atmospheric CO<sub>2</sub>. However, existing devices encounter stability issues (with only 1.6-10 h of continuous operation<sup>7,16,18</sup>) related to membrane fouling, electrode degradation and salt precipitation, hindering economic viability and integration with downstream CO<sub>2</sub> conversion technologies<sup>19</sup>. Consequently, there is a pressing need for the development of eDOC reactors that show long-term stability for the continuous capture of CO<sub>2</sub>.

Here we showcase a sustainable strategy for drop-in biochemical (chemically identical to their petro-derived peers) production from the ocean carbon sink, presenting a net-negative emission pathway for capturing and upgrading CO<sub>2</sub> from the ocean into biodegradable plastics. Our system integrates eDOC and CO<sub>2</sub> conversion processes with a biocatalytic approach facilitated by marine bacteria. For the eDOC process, we developed a solid electrolyte-based electrolysis reactor designed for the capture of CO<sub>2</sub> from natural seawater with a capture efficiency and energy input of >70% and ~3 kWh kgCO<sub>2</sub><sup>-1</sup>, respectively, under very dilute yet realistic DIC conditions (2.16 mM). The prototype device demonstrated remarkable durability by operating continuously for 536 h. during which it recovered ~6.54 l (under ambient conditions) of pure CO<sub>2</sub> gas from ~177 l of natural seawater. Concurrently, using a highly efficient and stable bismuth (Bi) catalyst, the captured CO<sub>2</sub> was electrocatalytically converted into pure formic acid, which was subsequently transformed by engineered Vibrio natriegens to yield succinic acid, an essential component for the production of poly(butylene succinate) (PBS) bioplastics. We achieved the efficient growth of microorganisms on formic acid substrates and produced succinate with a high yield of up to 1.37 g l<sup>-1</sup> using C<sub>1</sub> feedstock. By harnessing CO<sub>2</sub> captured from seawater as an alternative feedstock, our electro-biosynthesis system offers a viable pathway for decoupling raw chemical production from petrochemical production, driven by renewable electricity.

#### **Results**

#### Capture of CO<sub>2</sub> from seawater

Our ocean carbon recycling system, comprising both  $\rm CO_2$  capture and conversion processes, is illustrated in Fig. 1a. Regarding  $\rm CO_2$  capture, since the initial eDOC device was reported in  $\rm 2012^{15}$ , five main prototypes of eDOC devices have been developed in succession (see Supplementary Note 1 for details). However, current eDOC devices face critical challenges such as electrode fouling, membrane swelling and salt precipitation, which severely impair the durability and stability of the eDOC components and increase maintenance and replacement costs. We performed experiments to investigate the stability

of traditional BPMED cells (illustrated schematically in Fig. 1b) for continuous CO<sub>2</sub> extraction when natural seawater was used as a feedstock. Typically, the BPMED cells failed very quickly (Fig. 1c). During the operation process, Ca<sup>2+</sup> and Mg<sup>2+</sup> ions in the seawater preferentially react with OH<sup>-</sup> and form white precipitates of divalent hydroxides or carbonates. These precipitates are subsequently deposited within the base chamber, leading to blockage and an increase in cell resistance (Supplementary Fig. 6a). Furthermore, the presence of Ca<sup>2+</sup> and Mg<sup>2+</sup> ions in the seawater induces swelling of the bipolar membrane and subsequent fracture (Supplementary Fig. 6b), thereby contributing to the failure of the BPMED cells. Moreover, it is important to note that the stable operation of reported eDOC systems relies on the continuous supply of softened seawater, which necessitates co-location with large-scale, well-functioning and highly efficient operating desalination plants to support the practical application of the system (Supplementary Fig. 7). This poses additional challenges in terms of energy demand, land use, construction location and other related aspects. The development of an offshore, stand-alone system powered by renewables is crucial to advance the application of eDOC.

To increase the stability of eDOC and enable its integration with subsequent conversion applications, we designed a solid electrolyte-based eDOC system that overcomes these challenges and greatly extends its lifespan under direct natural seawater feeding conditions. Our design features the following: a bipolar membrane that directly separates the electrode chamber from the seawater and prevents ion exchange between the seawater and the electrolytes, thus preventing electrode fouling and salt precipitation. The acidification of seawater is accompanied by the production of a pure alkali solution, which eliminates the formation of undesired magnesium and calcium hydroxide precipitates that cause membrane swelling. The use of solid-state electrolytes in the chambers improves the ion conductivity and enhances the energy efficiency of eDOC (Supplementary Figs. 8 and 9). It uses a small amount of NaCl to enable the direct use of natural, unsoftened seawater as a feedstock and the continuous extraction of CO<sub>2</sub> in a highly integrated manner, offering increased economic viability compared with the pre-treatment process involved in obtaining softened seawater (Supplementary Note 2). The independent design of the cathode and anode chambers, without any ion exchange with seawater, not only resolves the challenge of electrode fouling but also facilitates facile adjustment of the current density applied to the electrode. This feature enables the device to be coupled with specific reactions, such as water splitting, thereby functioning as a versatile system for both synthesizing high-value chemicals and extracting CO<sub>2</sub> from seawater. Moreover, our design decouples the acidification and alkalization steps of seawater and restores the pH of the decarbonized seawater using an in situ prepared pure alkali solution, successfully overcoming the current challenges faced by hydroxide precipitation on the membrane.

Our solid electrolyte-based eDOC device prototype consists of five chambers (Fig. 2a). The cathode and anode chambers, where the hydrogen evolution reaction (HER) and oxygen evolution reaction (OER) occur, are separated by three compartments: the base, brine and acid chambers. These compartments are filled with solid electrolyte<sup>20</sup> to efficiently transport ions and minimize Ohmic loss across the entire device. The cathode and base chambers, as well as the anode and acid chambers, are separated by a bipolar membrane (BPM). A cation exchange membrane (CEM) and an anion exchange membrane (AEM) are positioned on either side of the brine chamber to realize selective ion passage. Commercial Pt/C and IrO<sub>2</sub> were used as electrocatalysts for the HER and OER, respectively. This HER/OER redox electrolysis generates an electric field within the middle chambers. In the base chamber, OH<sup>-</sup> released from the BPM combines with cations from the adjacent brine chamber to form the corresponding alkali that diffuses away in deionized (DI) water. Simultaneously, natural seawater is directed into another chamber, where it is injected with protons released from

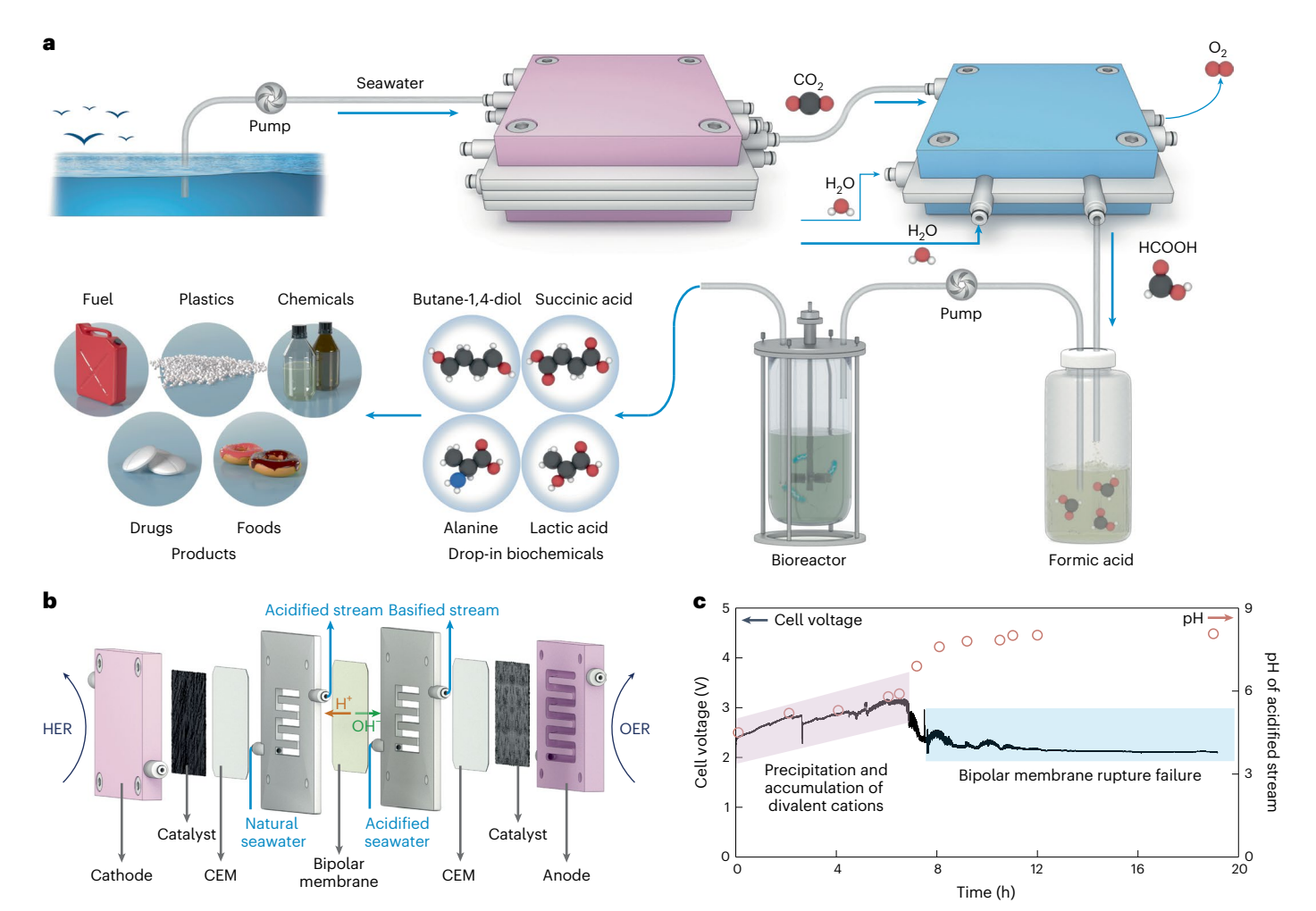


Fig. 1 | Proposed artificial oceanic carbon capture and upcycling system. a, Schematic illustration of the artificial ocean carbon recycling system that captures and converts oceanic  $CO_2$  into drop-in biochemicals through decoupled

electro-biocatalytic processes. **b**, Schematic illustration of traditional BPMED cells. **c**, Cell voltage and pH of the acidified stream as a function of operation time at a current density of 6 mA cm $^{-2}$  for more than 19 h.

another BPM to generate pH swings and achieve successful acidification. Consequently, the  $CO_2$ -carbonate equilibrium system ( $CO_2$ +  $H_2O \rightleftharpoons H^+ + HCO_3^- \rightleftharpoons H^+ + CO_3^{-2}$ ) in seawater is disrupted, leading to a shift towards  $CO_2$ . Next, the acidified seawater is pumped out of the acid chamber into hollow-fibre gas extraction membrane contactors, as illustrated in Supplementary Fig. 10, and the dissolved  $CO_2$  gas is extracted under vacuum pressure. To increase the purity of the  $CO_2$  gas, it is necessary to employ the same gas extraction module before the entry of the seawater into the acid chamber to remove dissolved gases such as  $O_2$  and  $O_2$ . Moreover, a cold-trap condenser is positioned between the membrane contactors and the vacuum pump to remove water vapour. Finally, the alkali produced in the base chamber is introduced into the  $CO_2$ -depleted acidified seawater to restore its initial pH, after which the mixture is discharged back into the ocean for efficient re-absorption of atmospheric  $CO_2$ .

We estimated the total DIC in natural seawater from Shenzhen Bay, China, using an alkalinity titration method. The DIC concentration was  $2.158\pm0.0342$  mM (Supplementary Note 3), comprising  $1.882\pm0.031$  mM  $HCO_3^-$ ,  $0.264\pm0.003$  mM  $CO_3^{2^-}$  and  $0.0121\pm0.0002$  mM  $CO_2$ , which is much higher than that in the atmosphere (417.2 ppm  $CO_2$  in  $2022)^1$ . We next established the equilibria between the concentrations of  $CO_2$ ,  $HCO_3^-$  and  $CO_3^{2^-}$  and pH (Supplementary Note 4) through a Bjerrum plot (Fig. 2b), which revealed that when the pH of acidified seawater drops below 4.92, more than 90% of

the DIC will be converted into  $CO_2$ . We then investigated the correlation between the pH of the acidified seawater and both the applied cell current density and the fresh seawater flow rate. As shown in Fig. 2c, a higher cell current density (j) was necessary to acidify seawater to the pH at which most carbonate and bicarbonate ions were converted into dissolved  $CO_2$  when the flow rate of seawater was increased. Based on the  $CO_2$  concentration–pH equilibrium, we further established the dependence of dissolved  $CO_2$  in acidified seawater on the cell voltage for a seawater flow rate of 330 ml h<sup>-1</sup>. In situ differential electrochemical mass spectrometry (DEMS; Fig. 2d) revealed that the  $CO_2$  signal (mass-to-charge ratio (m/z) = 44) emerged at ~2.55 V and gradually intensified until the cell voltage reached ~3.23 V, at which most of the DIC was efficiently converted into  $CO_2$ . There was no trace of impurity gases such as  $N_2$  (m/z = 14),  $O_2$  (m/z = 32) or  $H_2$  (m/z = 2), present during the experiment.

We also investigated the efficiency of  $CO_2$  capture and its associated energy consumption (Fig. 2e and Supplementary Figs. 11–13). At a lower operating cell current density, the acidification capacity of the reactor was insufficient, resulting in a low capture efficiency and high electrochemical energy consumption. Increasing the applied cell current density allowed the reactor to convert most of the DIC into  $CO_2$ , enhancing the capture efficiency of  $CO_2$  ( $\eta_{CO_2}$ ), but leading to an increase in electrochemical energy consumption. Moreover, the gas extracted from our reactor was confirmed to be high-purity  $CO_2$  by

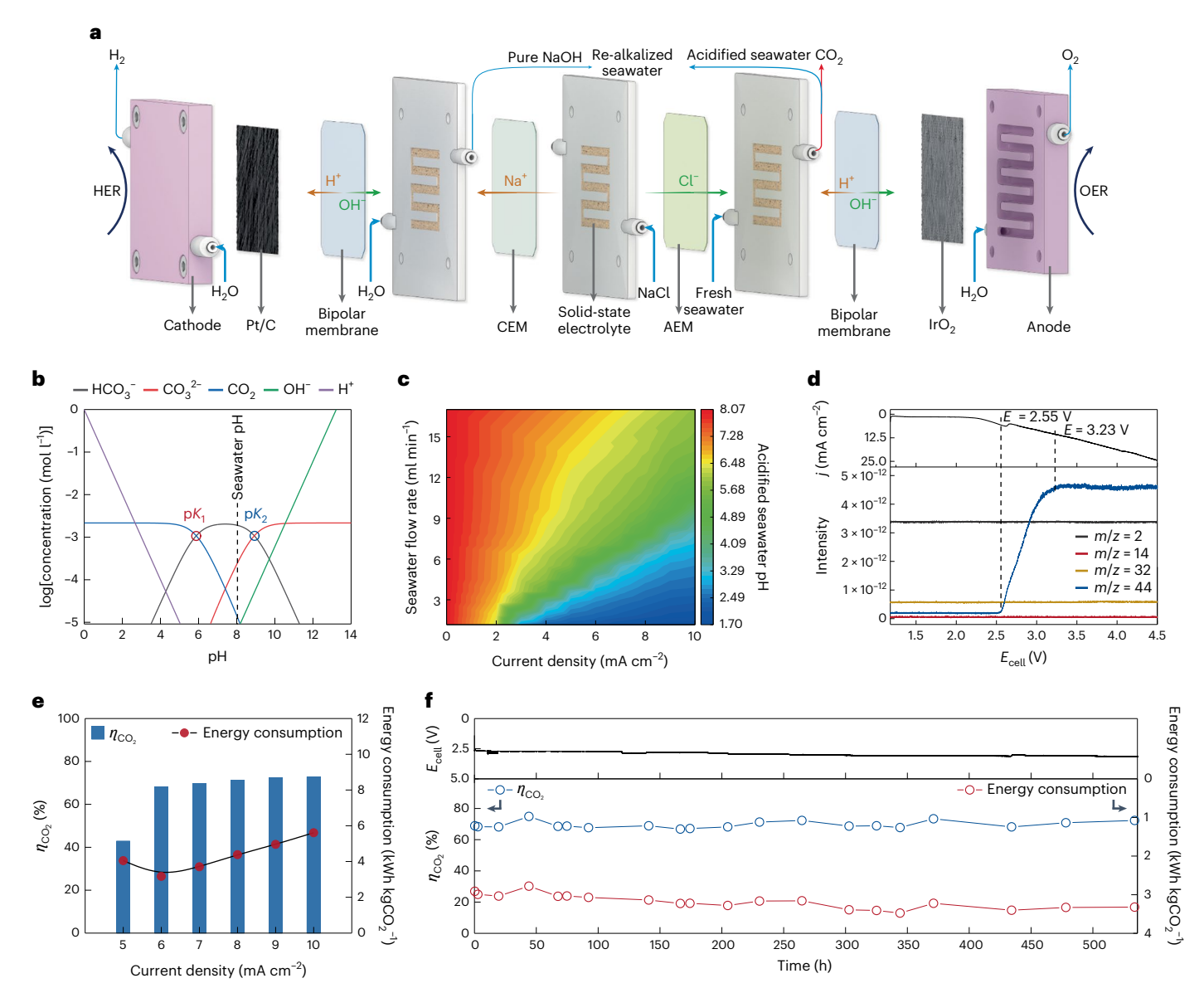


**Fig. 2**| **Capture of CO**<sub>2</sub> from seawater using our solid electrolyte electrolyser. **a**, Schematic illustration of our electrolyser designed for efficient  $CO_2$  capture from seawater. **b**, Bjerrum plot of log concentrations of  $HCO_3^-$ ,  $CO_3^{2^-}$ ,  $CO_2$ ,  $H^+$  and  $OH^-$  as a function of seawater pH. Note that when the pH is less than 4.92, the concentration of  $CO_2$  is more than 90% of the DIC.  $pK_1$  and  $pK_2$  denote the first and second acid dissociation constants of the carbonate system. **c**, pH of the acidified seawater output from the electrolyser as a function of the applied current density and the input seawater flow rate. **d**, In situ DEMS measurement of gas evolution during  $CO_2$  capture from seawater.  $E_{cell}$ , cell voltage. Top: current density as a function of applied  $E_{cell}$ . Bottom: mass spectrometry signals of the captured gas

at different  $E_{\rm cell}$ . Two experiments are conducted independently in the same voltage range.  $N_2$  is represented by m/z = 14 to avoid interference from the  $CO_2$  fragment at m/z = 28. **e**, Efficiency of  $CO_2$  capture ( $\eta_{CO_2}$ ) and electrochemical energy consumption at various cell current densities. **f**, Efficiency of  $CO_2$  capture ( $\eta_{CO_2}$ ) and electrochemical energy consumption during the continuous extraction of  $CO_2$  from seawater at a current density of 6 mA cm<sup>-2</sup> for more than 22 days. Top: variation of cell voltage with time. Bottom:  $CO_2$  capture efficiency and the corresponding energy consumption per kilogram of  $CO_2$  captured as a function of time.

mass spectrometry analysis (Supplementary Fig. 14). Importantly, upon the introduction of the  $^{13}\text{C}$ -labelled Na $_2$   $^{13}\text{CO}_3$  electrolyte into the acid chamber, our reactor generated pure  $^{13}\text{CO}_2$  gas (Supplementary Fig. 15), confirming that DIC in seawater was converted into CO $_2$ . To demonstrate the applicability of our design for mass recovery of CO $_2$ , we conducted a continuous electrolytic CO $_2$  production test using a 4 cm² solid electrolyte cell with a cell current density of 6 mA cm $^{-2}$  (lowest energy consumption) and a seawater flow rate of 330 ml h $^{-1}$ . As shown in Fig. 2f, this system exhibited remarkable durability, with  $\eta_{\text{CO}_2}$  and the energy consumption remaining at  $^{-70\%}$  and  $^{-3}$  kWh kgCO $_2$   $^{-1}$  (US\$60 tCO $_2$   $^{-1}$  for a cost of electricity from renewables of US\$0.02 kWh $^{-1}$ ), respectively, throughout continuous carbon capture operation from natural seawater for 536 h. Such continuous

operation resulted in a total production of -6.54 l of pure  $CO_2$  gas (under ambient conditions) from -177 l of natural seawater. The stability issues that plague existing devices, as evidenced by their limited operation time of only 1.6–10 h (refs. 7,16,18), are overcome in our superior design. This highlights the potential of our design for extended and more dependable operation (Supplementary Table 1). While some reported eDOC prototypes have lower energy consumption  $^{7,15}$ , they always employ artificial seawater as feedstock, which has a much higher DIC concentration (2.5–3.3 mM) than the natural seawater used in our work (-2.16 mM). Notably, our solid electrolyte reactor co-produces -0.9 moles of hydrogen fuel for every mole of  $CO_2$  recovered, reflecting substantial economic potential. We also sought to perform a robust techno-economic analysis of the capture of  $CO_2$  from natural seawater

according to previous studies<sup>21,22</sup> (see Supplementary Note 5 and Supplementary Table 2 for details). Our analysis revealed a cost of -US\$229.9 tCO<sub>2</sub><sup>-1</sup> for this system, which is highly competitive with current CO<sub>2</sub> capture technologies (Supplementary Table 3).

#### CO2 electrolysis

Following the capture of CO<sub>2</sub> from seawater, our next step involved the conversion of this captured CO<sub>2</sub> into energy-rich carbon intermediates, specifically formic acid, through electrocatalysis. We chose formic acid as a target product for the following reasons. According to previous studies<sup>23</sup>, formic acid has the highest profit per mole of electrons among the various products of the CO<sub>2</sub> reduction reaction (CO<sub>2</sub>RR). Furthermore, the bioconsumption of formic acid is preferred over other C<sub>1</sub> carriers because it is a proton-neutral process<sup>24</sup>. Moreover, it can be consumed by microbes as the sole carbon source for the production of biochemcials<sup>25</sup>. These benefits thus make the electrolysis of CO<sub>2</sub> to formic acid an attractive strategy. To optimize this conversion, we meticulously prepared a Bi-based metal-organic framework (MOF) catalyst with high activity, durability and ecofriendliness. The choice of Bi as the metal node was deliberate owing to its superior CO<sub>2</sub> reduction activity and pronounced selectivity for formate<sup>20,26,27</sup>. It is worth noting that most reported Bi-based catalysts have limitations in terms of activity and stability and are unable to match the extended stability period of our CO<sub>2</sub> capture system. Previous studies have shown that Bi-based catalysts can be stabilized during CO<sub>2</sub> electrolysis using organic surface modifiers such as ascorbic acid<sup>28</sup> or L-histidine<sup>29</sup>. In an effort to enhance the stability and activity of the Bi-based catalyst, we constructed a Bi-MOF using ellagic acid (EA) as the organic linker. Figure 3a illustrates our two-step synthesis of the catalyst (see Methods), involving the solvothermal synthesis of Bi<sub>2</sub>(EA)<sub>2</sub>(NMP)<sub>4</sub>(NO<sub>3</sub>)<sub>2</sub> (BEN; NMP = N-methylpyrrolidone), an atomically precise single-crystal material, followed by in situ reconstruction through electrochemical treatment at -1.2 V versus a reversible hydrogen electrode (RHE) for 30 min. We characterized the structure and morphology of BEN by various methods, including single-crystal X-ray diffraction (SCXRD), powder X-ray diffraction (PXRD; Fig. 3b), optical microscopy, scanning electron microscopy (SEM) and transmission electron microscopy (TEM; see Supplementary Figs. 16–18 for further details). The results revealed that BEN crystallizes in the triclinic space group  $P\bar{1}$  and exhibits a diamond-shaped morphology assembled from nanoscale filaments. In particular, Bi(III) is coordinated by EA, NMP and NO<sub>3</sub> ligands via deprotonated O atoms, forming a binuclear Bi(III) bridge and ultimately a one-dimensional coordination chain (Supplementary Fig. 19 and Supplementary Tables 4 and 5). The X-ray photoelectron spectroscopy (XPS) spectra of BEN and EA (Fig. 3c and Supplementary Fig. 20) confirmed the existence of Bi-O and C-N bonds in BEN.

To investigate the electronic and local coordination structures of Bi during the in situ electrochemical reduction of BEN, we conducted in situ X-ray absorption spectroscopy (XAS) measurements. Figure 3d shows the in situ Bi L<sub>3</sub>-edge X-ray absorption near-edge structure (XANES) spectra of BEN recorded at different applied potentials, along with the spectra of Bi metal and Bi<sub>2</sub>O<sub>3</sub> as references. The BEN spectra gradually approach that of the metallic Bi reference as the potential becomes more negative, indicating that the Bi nodes are partially reduced. The Fourier transform extended X-ray absorption fine structure (FT-EXAFS) spectra (Fig. 3e, the corresponding curves in k-space are shown in Supplementary Fig. 21) show peaks corresponding to the Bi-O and Bi-Bi paths, which indicates the formation of metallic Bi(0) from the binuclear Bi(III) bridge on the BEN surface during electrochemical reconfiguration. We also monitored the phase and state of Bi during reconstruction using in situ Raman spectroscopy. As shown in Fig. 3f, applying a negative potential of −1.2 V versus RHE increased the intensity of the two peaks corresponding to the stretching vibrations of the Bi-Bi signals, namely Eg and Alg. After undergoing in situ electrochemical reconstruction, Bi nanocrystals were produced that were uniformly dispersed on BEN, as shown by TEM (Fig. 3g) and scanning transmission electron microscopy energy-dispersive X-ray spectroscopy (STEM-EDS) mapping (Fig. 3h). K and L correspond to the atomic shell from which the characteristic X-ray was emitted. We also confirmed the presence of the BEN matrix after electroreduction by matrix-assisted laser desorption ionization time-of-flight mass spectrometry (MALDI-TOF MS; Fig. 3i). These results demonstrate that we successfully prepared Bi-decorated BEN, that is, the Bi-BEN catalyst, via an in situ electrochemical transformation.

To evaluate the catalytic performance of Bi-BEN in the production of formate from CO<sub>2</sub>, we used a standard three-electrode flow cell system with 0.5 M KHCO<sub>3</sub> as the electrolyte (see Methods). The only liquid product obtained with the Bi-BEN catalyst during the CO<sub>2</sub>RR was formate, with over 90% selectivity within the potential range of -0.83 to -1.37 V versus RHE, along with trace amounts of gaseous H<sub>2</sub> and CO products (Fig. 4a). The maximal Faradaic efficiency (FE) for formate reached 96% at -400 mA cm<sup>-2</sup> and remained greater than 90% even at -800 mA cm<sup>-2</sup>. Thus, the Bi-BEN catalyst maintained a superior activity and selectivity towards formate, even at a high current density, compared with commercial Bi nanoparticles (Bi NPs; Supplementary Fig. 22). A formate partial current density ( $j_{\text{formate}}$ ) of -720 mA cm<sup>-2</sup> was achieved by Bi-BEN at around -1.37 V versus RHE, whereas the Bi NPs only delivered a  $j_{\text{formate}}$  of -338 mA cm<sup>-2</sup> at around -1.30 V versus RHE (Fig. 4b). Bi-BEN also outperformed previous Bi-based electrocatalysts (Fig. 4c and Supplementary Table 6). Compared with the Bi NPs, Bi-BEN also showed a reduced overpotential under  $the same \emph{j}_{formate} conditions, proving that its activity is greatly enhanced.$ A stability test performed on the Bi-BEN catalyst revealed that the FE of formate remained at around 95%, even after continuous electrolysis at a current density of -200 mA cm<sup>-2</sup> for 23 h, without a voltage drop (Fig. 4d). The stability of the Bi NPs was found to be inferior, their FE decreasing over a period of 8 h at a current density of -200 mA cm<sup>-2</sup> (Supplementary Fig. 23). Analysis of Bi-BEN after the catalytic process reconfirmed its structural stability (Supplementary Figs. 24 and 25). In addition, DEMS revealed that the Bi-BEN catalyst had a higher onset potential for H<sub>2</sub> (Fig. 4e) and CO (Fig. 4f) than did the Bi NPs. To account for the potential difference in the electrochemically active surface area (ECSA) of Bi-BEN and Bi NPs as well as the resulting variations in activity, we estimated the ECSAs via cyclic voltammetry and ECSA-normalized  $j_{\text{formate}}$  (Supplementary Figs. 26 and 27). These results show that the intrinsic activity of Bi-BEN surpasses that of Bi NPs. We suppose that the higher activity of Bi-BEN can be attributed to the electrochemical reconfiguration process, which results in the formation of an organic ligand-modified Binanocrystal (Fig. 3a). This structural modification improves the stability of crucial reaction intermediates involved in the formation of formate and suppresses the HER and generation of CO.

We conducted a comprehensive investigation to determine the mechanism of CO<sub>2</sub> reduction to formate on the Bi-BEN catalyst. Initially, we performed a kinetic analysis, using Tafel plots, to scrutinize the rate-determining steps. Our results revealed a Tafel slope of 125 mV dec<sup>-1</sup> for Bi-BEN, suggesting that the initial electron transfer step, which is responsible for producing surface-adsorbed CO<sub>2</sub> (\*CO<sub>2</sub>-), serves as the rate-determining step (Supplementary Fig. 28 and Supplementary Table 7)30,31. Moreover, compared with bare Bi NPs, which have a Tafel slope of  $275\,\mathrm{mV}\,\mathrm{dec^{-1}}$ , Bi-BEN shows faster formate generation kinetics<sup>32,33</sup>. To investigate the process at the molecular level, we used in situ attenuated total reflection surface-enhanced infrared absorption spectroscopy (ATR-SEIRAS). As the cathodic potential was increased, absorption peaks associated with HCOO\* species and their vibrations were observed (Fig. 4g)34-37. Notably, HCOO\* was observed on both Bi-BEN and Bi NPs, but the former needed a lower potential, indicating higher HCOO\* coverage. These HCOO\* peaks vanished when the potential was removed, revealing their dependency on potential (Supplementary Fig. 29). No detectable \*CO fingerprint infrared band was detected, confirming the limited selectivity of both

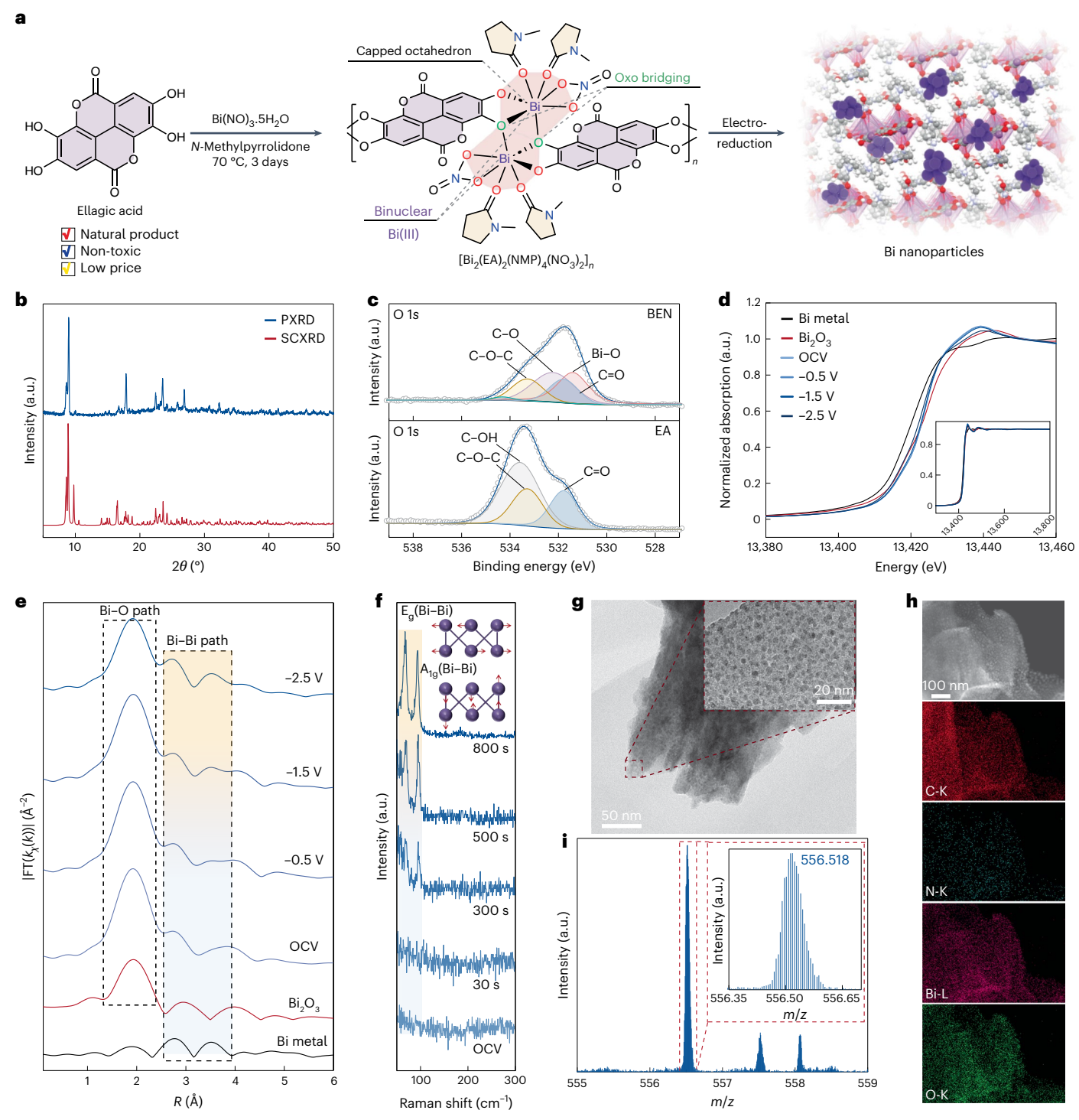


**Fig. 3** | **Structural characterization of Bi-BEN. a**, Schematic illustration of the synthesis of Bi-BEN. **b**, PXRD and SCXRD patterns of single crystals of BEN. **c**, High-resolution XPS O 1s spectra of BEN and EA, with the deconvolution spectra of the different structural elements. **d**,**e**, In situ Bi  $L_3$ -edge XANES (**d**) and EXAFS (**e**) spectra of BEN at different applied potentials. The spectra of Bi $_2$ O $_3$  and Bi foil are shown as references. Inset in **d**: full XANES spectrum, with axis labels the same as those in the main plot. The dashed boxes and shaded region respectively highlight the Bi-O and Bi-Bi coordination paths in **e**. **f**, In situ Raman spectra of BEN as a function of reaction time at -1.2 V versus RHE. Shaded region highlight

the Bi–Bi vibrational modes. Inset: Raman vibrational signals of Bi–Bi, with the top and bottom corresponding to the  $E_{\rm g}$  and  $A_{\rm lg}$  modes, respectively.  ${\bf g}$ , TEM image of Bi-BEN. Inset: magnification of the TEM image, showing that Bi nanocrystals are uniformly dispersed on BEN.  ${\bf h}$ , STEM-EDS mapping of C, N, Bi and O in the Bi-BEN catalyst. The scale bar applies to all images. K, K-edge; L, L-edge.  ${\bf i}$ , MALDI-TOF MS spectrum of Bi-BEN. Inset: enlarged view of the main peak region. The representative images in  ${\bf g}$  and  ${\bf h}$  were reproduced in at least three independent experiments with similar results. All potentials have been calibrated to the RHE scale. OCV, open-circuit voltage; a.u., arbitrary units.

Bi-BEN and Bi NPs for CO. Moreover, during in situ Raman analysis, we also observed a strong peak related to the  $v_{C-H}(HCOO^-)$  stretching vibration, its intensity matching the rate of formate formation (Supplementary Fig. 30). During the in situ reconstruction of BEN,

depolymerization of the Bi sites results in an abundance of free ligands, including EA and NMP, in the local environment. In this Article, we propose that ligand modification of the Bi nanocrystals stabilizes the key HCOO\* intermediate, enabling high activity even at high current

densities. An investigation of the strength of the interactions between the ligands and Bi (Supplementary Fig. 31) showed that EA is adsorbed much more readily than NMP, which is essentially non-adsorbing.

The enhanced catalytic performance of Bi modified with EA and NMP was explored through theoretical simulations. The adsorption energies of molecules of EA and NMP on the Bi(001) surface were calculated, revealing that EA has a lower adsorption energy (Supplementary Fig. 32). These results are consistent with the experimental observations (Supplementary Fig. 31), suggesting that EA strongly influences the catalytic performance of Bi. Based on these findings, Gibbs free-energy diagrams were constructed to evaluate the differences in the catalytic performance of pure Bi(001) and EA@ Bi(001) (Fig. 4h and Supplementary Fig. 33). The profiles show that the loading of EA enhances CO<sub>2</sub> adsorption and lowers the limiting potential of the first step of HCOOH generation via HCOO\* intermediates, which aligns closely with the experimental results. The formation of a hydrogen bond between EA and the HCOO\* group stabilizes the HCOO\* intermediate by providing additional electrons. The change in electron transfer after EA loading was confirmed through the difference in charge density, which shows an increase in electrons obtained from the HCOO\* group (Supplementary Fig. 34). Projected density of states calculations indicated a more stable system, which is consistent with enhanced CO<sub>2</sub> reduction activity of the Bi metal catalyst towards formate formation after ligand modification (Supplementary Fig. 35 and Supplementary Table 8). In summary, the combination of experimental and computational approaches has provided a comprehensive understanding of the CO<sub>2</sub>-to-formate conversion mechanism on the Bi-BEN catalyst, shedding light on the critical role of EA modification in enhancing the catalytic performance.

# Microorganisms use formate as the sole carbon source for fermentation

In the CO<sub>2</sub> reduction process with the Bi-BEN catalyst, we encountered a challenge: the formate products contained concentrated electrolyte salts due to the presence of a 0.5 M KHCO<sub>3</sub> electrolyte solution. This led to the need for energy-intensive separation and purification steps to obtain bioconsumable feedstocks. To tackle this issue and directly produce pure formic acid (HCOOH), we employed a solid electrolyte reactor, a technology that we previously developed for the synthesis of high-purity formic acid<sup>20</sup>. In this reactor (Fig. 5a), the HCOO<sup>-</sup> anions generated during CO<sub>2</sub> reduction and driven by an electric field move through an AEM towards the central solid electrolyte channel. Simultaneously, protons generated by water oxidation on the anode side traverse a CEM. The solid electrolyte that we used conducts protons. facilitating the recombination of ions to form HCOOH, which then diffuses into DI water and flows out of the reactor. Our experiments, which were conducted with a DI water flow rate of 108 ml h<sup>-1</sup> and the Bi-BEN catalyst loaded on a 4 cm<sup>2</sup> electrode, yielded promising results. At a cell current density of 75 mA cm<sup>-2</sup> (equivalent to a cell current of 300 mA), we achieved a peak HCOOH FE of around 92% (Fig. 5b). Only HCOOH was detected in the liquid product via <sup>1</sup>H and <sup>13</sup>C nuclear magnetic resonance (NMR) spectroscopy (Supplementary Fig. 36).

#### Fig. 4 | CO<sub>2</sub>RR performance and mechanistic studies of Bi-BEN and Bi NPs.

**a**, FEs for all CO<sub>2</sub>RR products at different current densities and the corresponding j–V curves for the Bi-BEN and Bi NP catalysts in a flow cell. **b**, Variation in j<sub>formate</sub> with applied potential over the Bi-BEN and Bi NP catalysts. **c**, Comparison of j<sub>formate</sub> values and the working potential range of Bi-based catalysts reported in the literature. Bi-PNS, bismuth porous nanosheets<sup>48</sup>; j-BiNSs, jagged bismuth nanosheets<sup>49</sup>;  $Sn_{0.80}Bi_{0.20}@Bi-SnO_{x}$ , the core is crystalline  $Sn_{0.80}Bi_{0.20}$  alloy and the shell is Bi-doped amorphous  $SnO_{x}$  (ref. 50); 3D Bi-ene-A/CM, three-dimensional open network of interconnected bismuthene arrays<sup>51</sup>; Bismuthene nanosheets<sup>52</sup>; Bi-ene-NW, self-supported large-size three-dimensional porous conductive network of bismuthene<sup>27</sup>; Bi@Sn NPs, core-shell nanoparticles (Bi core and Sn shell)<sup>53</sup>; BBS, the Bi nanosheets with the edge defect sites coordinated with S via electrochemical reconstruction of Bi<sub>19</sub>Br<sub>3</sub>S<sub>27</sub> nanowires<sup>54</sup>; Bi MP, angular-shaped

This observation further demonstrates the stability of the organic ligands within the Bi-BEN catalyst. Further increasing the cell voltage, we achieved a maximal formic acid partial current density of 108 mA cm<sup>-2</sup>, resulting in a solution of pure formic acid with a concentration of 0.065 M (Supplementary Fig. 37). The use of <sup>13</sup>C-labelled CO<sub>2</sub> also confirmed that HCOOH was indeed produced through CO<sub>2</sub> reduction (Supplementary Fig. 38). Scaling up the device using a 25 cm<sup>2</sup> solid electrolyte (Supplementary Fig. 39) achieved the ultrastable production of HCOOH in solution over a period of 20 days (480 h), which is compatible with our continuous CO<sub>2</sub> capture system. With a cell current of 1.2 A and DI water flow rate of 42 ml h<sup>-1</sup>, we maintained an HCOOH FE above 82% without a appreciable drop in voltage, leading to a total production of around 20.16 l of approximately 0.45 M pure HCOOH (Fig. 5c.d). This result surpasses the performance of previously reported HCOOH-selective electrocatalysts (Supplementary Table 9) and further highlights the critical role of EA in stabilizing Bi catalysts.

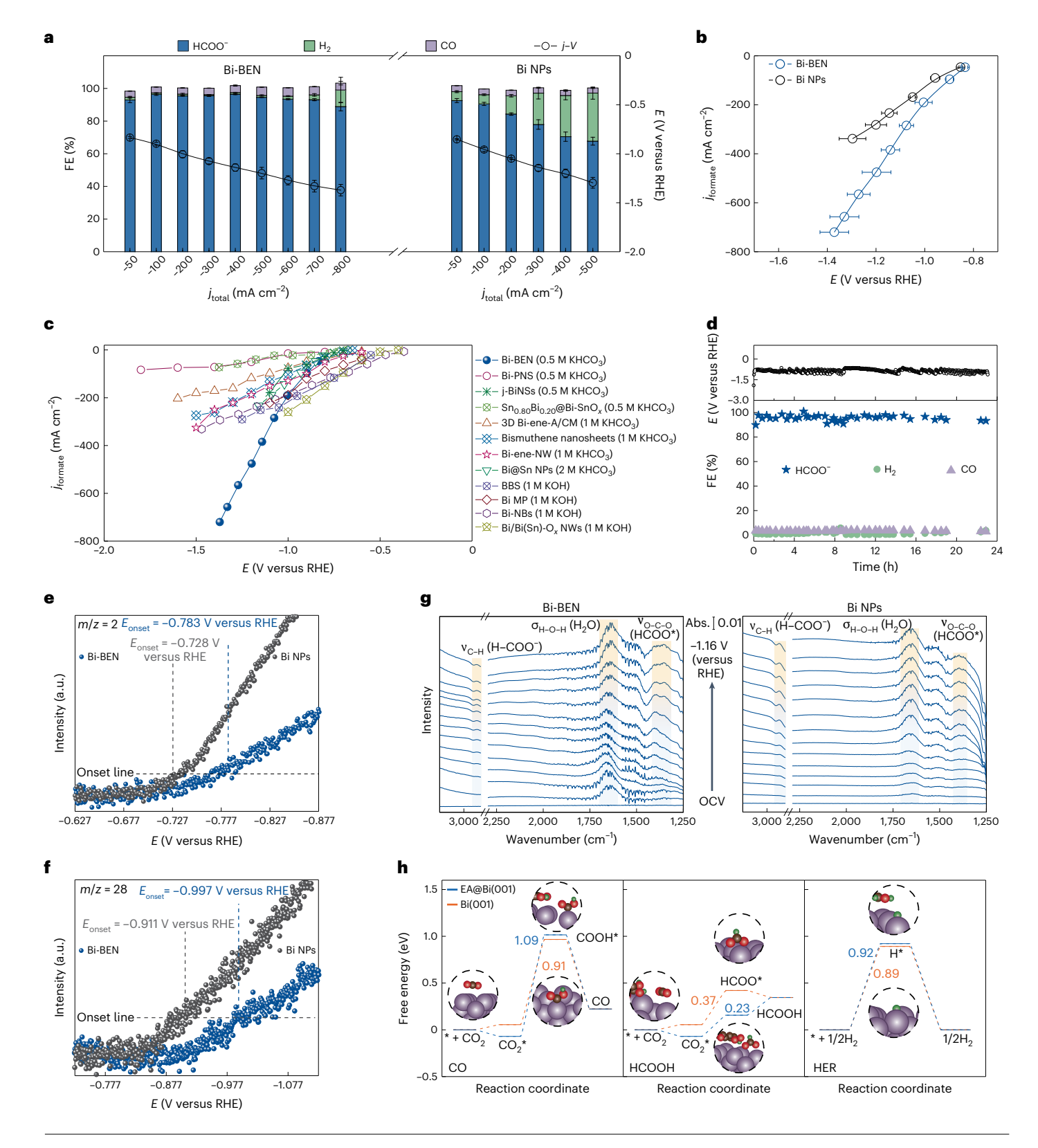
The pure and concentrated HCOOH derived from ocean-captured CO<sub>2</sub> can serve as a sustainable feedstock for microbial fermentation. Compared with inert CO<sub>2</sub>, microbes exhibit a greater ability to use HCOOH as feedstock. This makes HCOOH a prime candidate for the bioproduction of valuable chemicals. V. natriegens (ATCC 14048), a marine microorganism with a high growth rate (doubling time < 10 min) and substrate consumption rate <sup>38,39</sup>, is a promising microbial chassis for biotechnology. Recently, V. natriegens was found to have intrinsically high HCOOH tolerance and metabolic capacity<sup>25</sup>. Therefore, it could be a great candidate for use with HCOOH as the sole carbon and energy source for the production of biochemicals. An adaptive laboratory-evolved strain with enhanced HCOOH tolerance was selected as the starting strain<sup>25</sup> in this study. The tetrahydrofolate (THF) cycle is emerging as a promising HCOOH assimilation pathway due to its enzymatic oxygen tolerance, energy efficiency and self-sustaining operation 40,41. To further enhance the metabolic activity of HCOOH, we introduced three enzymes, namely, Methylobacterium extorquens formate-THF ligase (Ftl), methenyl-THF cyclohydrolase (Fch) and methylene-THF dehydrogenase (Mtd; Fig. 5e), to yield the strain XG251 (ref. 40). The energy required for microbial metabolism is produced from the oxidation of formate to CO<sub>2</sub> by formate dehydrogenase (Fdh)<sup>25</sup>. These gene-mediated pathways for formate assimilation and energy production facilitate formate metabolism in V. natriegens, enabling its growth and product synthesis using formate as both a carbon and energy source.

Succinate is one of the top 12 bio-based platform chemicals, serving as a precursor for the synthesis of numerous chemical products  $^{42}$ , including PBS, a representative biodegradable plastic  $^{43}$ . *V. natriegens* possesses a strong innate ability to produce succinate from glucose  $^{44,45}$ . To evaluate the capability of the engineered strains to convert formate into succinate, *V. natriegens* was inoculated into rich medium containing 441 mM formate and cultured to an optical density at 600 nm (OD  $_{600}$ ) of 1.0–1.5. The cells were then collected, washed and resuspended in minimum medium containing 441 mM formate (the sole organic) at OD  $_{600}$  values of 1, 3, 5 and 10 for succinate production. An OD  $_{600}$  of 10 was determined to be optimum for subsequent fermentation tests

Bi microparticles<sup>55</sup>; Bi-NBs, ultralong and thin Bi nanobelts<sup>56</sup>; Bi/Bi(Sn)-O<sub>x</sub> NWs, Sn doped Bi/BiOx nanowires<sup>57</sup>. **d**, Stability test of Bi-BEN for more than 23 h in a flow cell at a current density of -200 mA cm<sup>-2</sup>. Top: current density as a function of time. Bottom: FEs for all CO<sub>2</sub>RR products as a function of time. **e**, **f**, In situ DEMS measurements of H<sub>2</sub> (**e**) and CO (**f**) production during the CO<sub>2</sub>RR on Bi-BEN and Bi NP catalysts. **g**, In situ ATR-SEIRAS spectra of Bi-BEN and Bi NPs recorded at various applied potentials ranging from the OCV to -1.16 V versus RHE. v and  $\sigma$  denote stretching and bending vibrational modes, respectively. **h**, Calculated free-energy diagrams for the CO<sub>2</sub>RR to CO, HCOOH and HER on pure Bi(001) and EA@Bi(001) surfaces. In **a** and **b**, the data are presented as the mean  $\pm$  standard deviation (s.d.) of three independent measurements (n = 3). All potentials have been calibrated to the RHE scale.

according to the cell growth rate and rate of synthesis of succinic acid (Supplementary Fig. 40). As shown in Fig. 5f, the engineered strain XG251 grew in the formate-supplemented medium but not in the absence of formate, indicating that formate, rather than residual nutrients from the rich medium, supported cell growth. In contrast, the wild-type V. natriegens strain failed to grow under the same conditions with formate. As shown in Fig. 5g, strain XG251 produced succinate with a titre of  $0.662 \, \mathrm{g} \, \mathrm{I}^{-1}$ , representing an improvement of 48.5% over the control

strain. In addition, the succinate conversion yield increased by 18%, from 0.03 to 0.035 g per g HCOOH (Fig. 5h and Supplementary Fig. 41), probably due to the enhanced formate utilization activity resulting from the introduction of the Ftl-Fch-Mtd metabolic pathway. Interestingly, strain XG251 continued to produce succinate over a test period of 16 h, whereas the control strain showed lower succinate production at the end of this period (Fig. 5g,h). No detectable succinate was produced by strain XG251 in the absence of formate, further confirming that



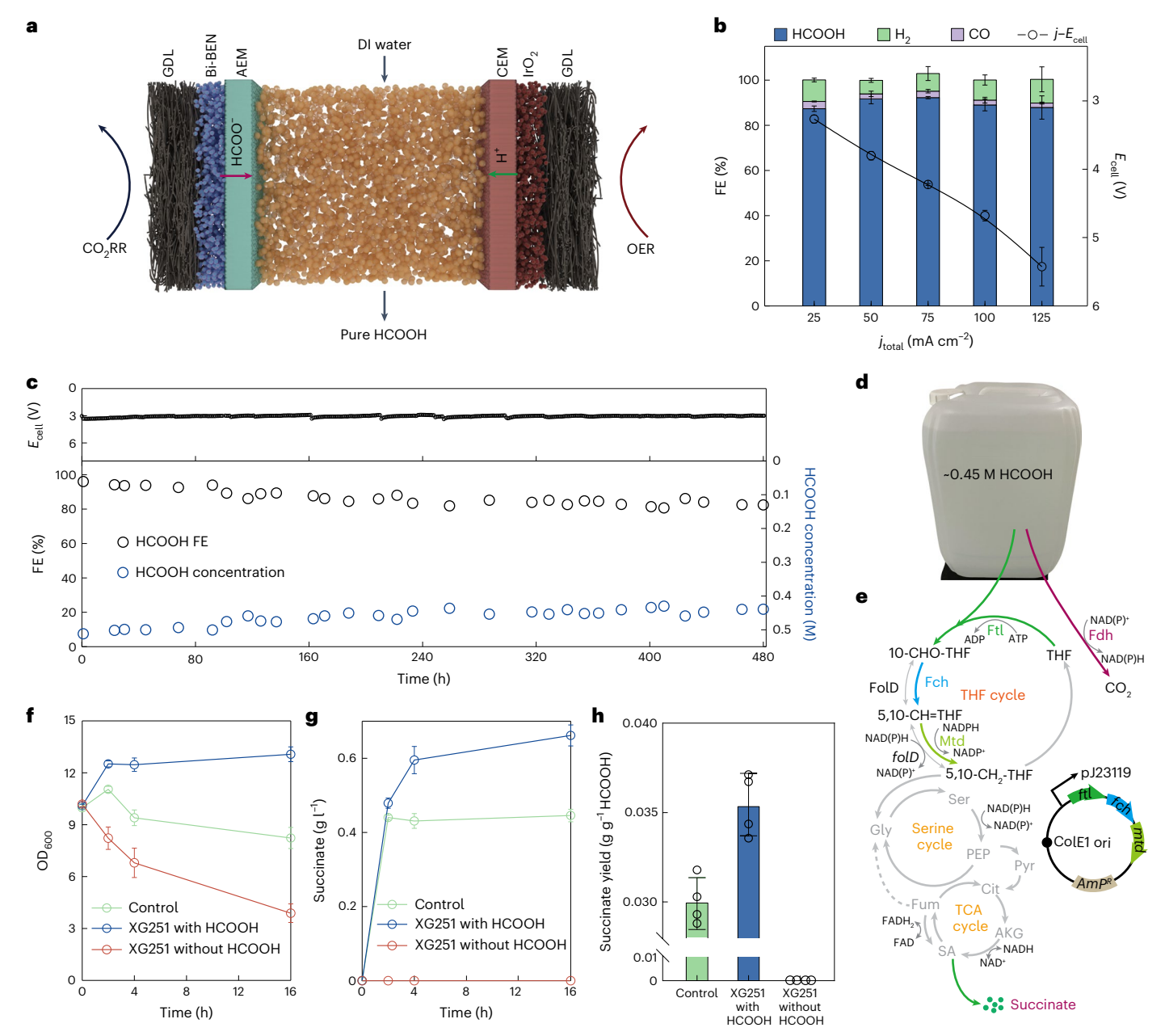


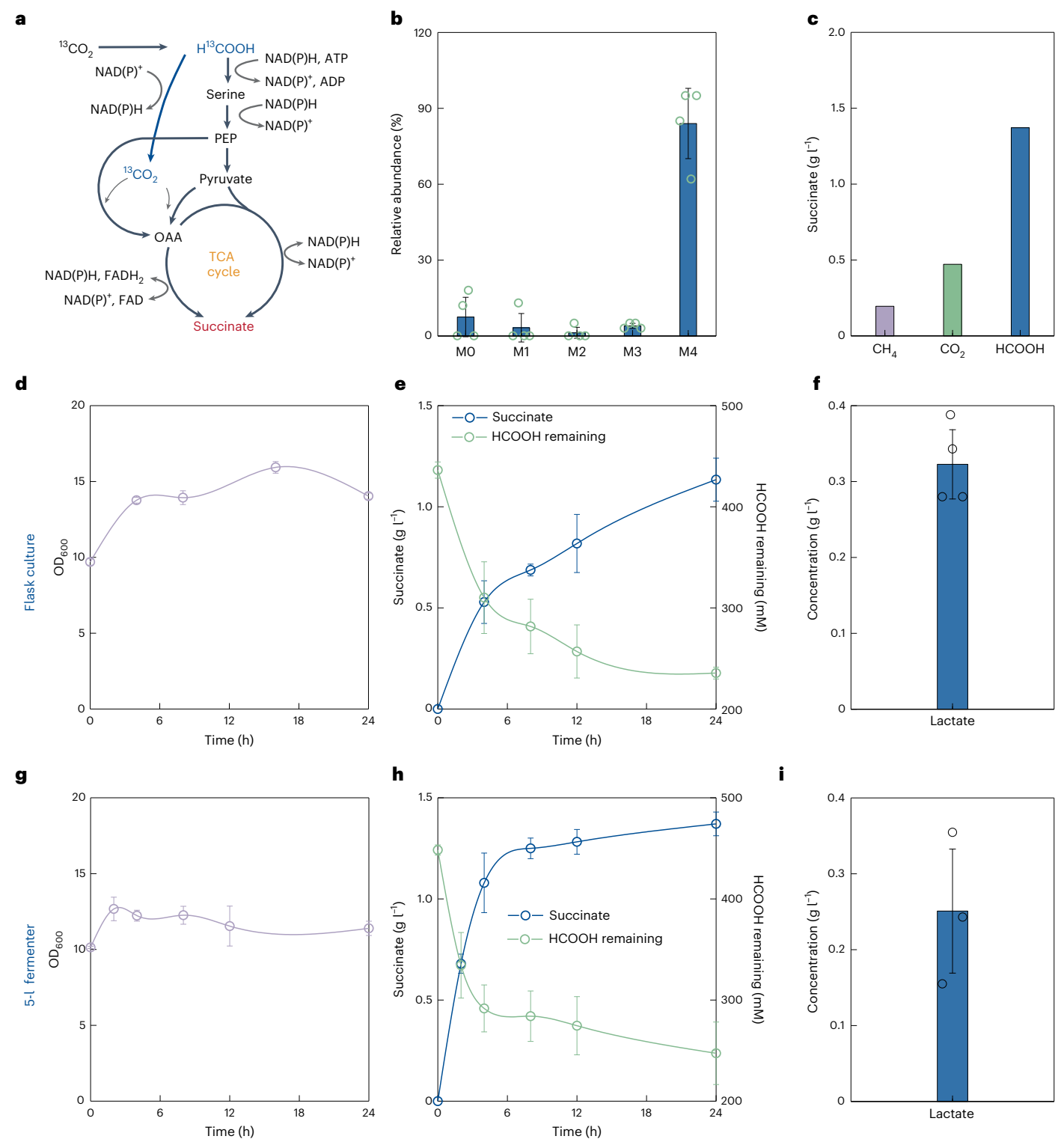
**Fig. 5** | **Electrochemical production of formic acid and microbial conversion to succinate. a**, Schematic of a solid electrolyte reactor for the production of pure HCOOH. **b**, FEs of all CO $_2$ RR products at different current densities and the corresponding j– $F_{cell}$  curve for the Bi-BEN catalyst in a solid electrolyte reactor (an electrode area of 4 cm $^{-2}$  was used). The data are presented as the mean  $\pm$  s.d. from three independent measurements (n = 3). **c**, Long-term production of pure formic acid with the Bi-BEN catalyst at a current of 1.2 A in the solid electrolyte reactor for 20 days (480 h) without iR (current–resistance) correction of the cell voltage (an electrode area of 25 cm $^2$  was used). **d**, Photograph of the pure formic acid product. **e**, The recombinant tetrahydrofolate cycle was established in V. natriegens. Dark green, Ftl, formate-THF ligase; blue, Fch, methenyl-THF cyclohydrolase; light green, methylene-THF dehydrogenase; magenta: Fdh, formate dehydrogenase. The grey arrows represent endogenous pathways. The designed and used recombinant plasmids are displayed in the lower right

corner. **f-h,** Growth curves (**f**), succinate formation (**g**) and succinate yields (**h**) obtained in wild-type V.natriegens and the XG251 strain cultured in minimal medium with and without formate as the sole carbon and energy source or without formate as a carbon source. The data are presented as the mean  $\pm$  s.d. from four independent measurements (n = 4). GDL, gas diffusion electrode; ATP, adenosine triphosphate; ADP, adenosine diphosphate;  $AmP^R$ , ampicillin resistance gene; FolD, bifunctional methylenetetrahydrofolate dehydrogenase; THF, tetrahydrofolate; PEP, phosphoenolpyruvate; Pyr, pyruvate; Ser, serine; Gly, glycine; Fum, fumarate; Cit, citrate; AKG,  $\alpha$ -ketoglutaric acid; SA, succinate; FADH<sub>2</sub>, reduced flavin adenine dinucleotide; NAD+, nicotinamide adenine dinucleotide; NAD+, nicotinamide adenine dinucleotide phosphate; NADP+, nicotinamide adenine dinucleotide phosphate; NADP+, nicotinamide adenine dinucleotide phosphate; TCA cycle, tricarboxylic acid cycle; ColE1 ori, ColE1 origin of replication.

formate was the sole substrate responsible for cell growth and chemical production, rather than residual organics from the culture medium (Fig. 5f,g). These results demonstrate that the engineered strain XG251 efficiently converts HCOOH into succinate.

We next investigated the integration of oceanic CO<sub>2</sub>-derived HCOOH into succinate production. We prepared <sup>13</sup>C-labelled H<sup>13</sup>COOH

using our solid electrolyte reactor. To validate succinate production through HCOOH assimilation, H<sup>13</sup>COOH was used as the sole carbon and energy source for fermentation (Fig. 6a). After cultivation for 24 h, the <sup>13</sup>C-labelled succinate was measured by gas chromatography–mass spectrometry (GC–MS). As depicted in Fig. 6b, the mass isotopmer distributions of succinate supporting different numbers of



 $\label{eq:continuous} \textbf{Fig. 6} \ | \ \textbf{Using formate synthesized from CO}_2 \ for microbial production of succinate. a, Schematic of the microbial production of succinate from CO}_2 \ via formate. OAA, oxaloacetate. b, Relative abundance of mass isotopomers of succinate from XG251 cells. Mx represents succinate with $x^{13}$C atoms $(x=0-4)$. c, Comparison of the production of succinate from HCOOH as the sole carbon source and other C1 chemicals previously reported in the literature $8.59$. d, Growth of XG251 cells within a timeframe of 24 h in a 50-ml flask. e, Succinate production and HCOOH consumption in XG251 cells within a timeframe of 24 h in a 50-ml$ 

flask. **f**, Concentration of lactate byproduct after 24 h of fermentation in a 50-ml flask. **g**, Growth of XG251 cells within a timeframe of 24 h in a 5-l fermenter. **h**, Succinate production and HCOOH consumption in XG251 cells within a timeframe of 24 h in a 5-l fermenter. **i**, Concentration of lactate byproduct after 24 h of fermentation in a 5-l fermenter. For **b** and **d**–**f**, the data are presented as the mean  $\pm$  s.d. from four independent measurements (n = 4); for **g**–**i**, the data are presented as the mean  $\pm$  s.d. from three independent measurements (n = 3).

 $^{13}$ C (M4, M3, M2, M1 and M0, where Mx represents succinate with  $x^{13}$ C atoms) were 84%, 4%, 1,25%, 3,25% and 7,5%, respectively. This finding indicates that the majority of the carbon in succinate is synthesized through HCOOH metabolism. We next optimized the culture conditions to further improve succinate production from HCOOH. In previous studies, resting cells were used as biocatalysts to increase succinate production via the use of glucose<sup>46</sup>. We cultivated anaerobic stationary-phase cells of strain XG251 as biocatalysts, starting with an OD<sub>600</sub> of around 10, to convert marine CO<sub>2</sub>-derived HCOOH, as the sole carbon and energy source, into succinate. The biomass of the resting cells increased by 64.3% during fermentation (Fig. 6d), indicating that the cells exhibited good activity during fermentation, which is critical for further industrial application. In the reaction flask, succinate production reached 1.13 g l<sup>-1</sup> (Fig. 6e), the rate of succinate production reached 0.072 g l<sup>-1</sup> h<sup>-1</sup> and the yield of succinate from HCOOH was 0.121 g g<sup>-1</sup>HCOOH (Supplementary Fig. 42). In addition, our analysis revealed a lactate concentration of 0.323 g l<sup>-1</sup> during fermentation (Fig. 6f). The energy conversion efficiency of the hybrid electro-biosystem for the production of succinate reached 7.12% (Supplementary Note 6).

As demonstrated above and in our previous study<sup>47</sup>, electrolyser stacks can be easily scaled up for practical application. To demonstrate the practicality and viability of this electro-biosystem, we sought to extend our bioreactor for scale-up biosynthesis. We switched from using laboratory-scale conical bottles to using 1- or 5-l fermenters for biocatalysis (Supplementary Fig. 43). In a 1-I fermenter, the XG251 strain exhibited continuous proliferation over 24 hand achieved a competitive succinate yield of 1.16 g l<sup>-1</sup> (Supplementary Fig. 44a,b). The corresponding rate of succinate production reached  $0.049 \,\mathrm{g}\,\mathrm{l}^{-1}\,\mathrm{h}^{-1}$ , and the yield of succinate from HCOOH was 0.13 g g<sup>-1</sup>HCOOH (Supplementary Fig. 44c). Next, we increased the fermenter size from 1 to 5 l, achieving a rate of succinate production of 1.37 g l<sup>-1</sup> (Fig. 6h). During fermentation, bacterial growth increased by 25%, accompanied by lactate production of 0.25 g l<sup>-1</sup> (Fig. 6g,i). Notably, lactate is a important product of the process, serving as a vital precursor for the synthesis of biodegradable polylactic acid. It is also a key bio-alternative chemical within the bioplastics industry and is derived from our system, highlighting its importance in sustainable material development. The corresponding rate of succinate production was 0.057 g l<sup>-1</sup> h<sup>-1</sup>, the yield of succinate from HCOOH was 0.15 g g<sup>-1</sup>HCOOH and the pH remained stable during fermentation (Supplementary Figs. 45 and 46). These results show that our bioreactor can be easily scaled up for production while maintaining substantial yields, exemplifying the practical potential of this system. The level of succinate production is greater than that reported for bio-succinate production when other C<sub>1</sub> substrates were used as the sole carbon and energy source (Fig. 6c and Supplementary Table 10). Notably, the integration of the three modules has been successfully demonstrated at a laboratory scale, finally outputting 1.22 g l<sup>-1</sup> succinate (Supplementary Fig. 47), which can be further optimized and integrated.

Plastics are ubiquitous in modern society, but they also cause serious global problems that affect ecosystems because of their resistance to decomposition. This has spurred research into biodegradable alternatives that can be broken down and ultimately decomposed into CO<sub>2</sub> by microorganisms. By leveraging the well-established principle underlying PBS synthesis from succinate, the use of the drop-in bio-alternative in the synthesis of PBS serves as a compelling demonstration of the practical potential of this system, highlighting the comparability and equivalency of our biochemical products to industrial synthetics. As displayed in Supplementary Figs. 48-54 and Supplementary Tables 11 and 12, high-quality PBS products could be obtained using our oceanic CO<sub>2</sub>-derived succinate. This highlights the practicality of drop-in biochemicals from our system. These results demonstrate that the XG251 strain is a promising biocatalyst for using HCOOH as the sole carbon source for producing succinate, offering opportunities for the development and scale-up of CO<sub>2</sub>-driven HCOOH biorefineries. We believe that our research will usher in an era of biochemical synthesis using ocean carbon sinks, leading to the development of a large number of carbon-negative products in the foreseeable future.

#### Conclusions

In this study, we extracted CO<sub>2</sub> from natural seawater to synthesize biodegradable plastics via a hybrid electro-biosystem. We developed a solid electrolyte-based electrolysis reactor that captures CO<sub>2</sub> from oceanic carbon sources with high energy efficiency and stability. Remarkably, this reactor produced around 6.54 l of CO<sub>2</sub> gas from around 177 l of natural seawater during continuous operation for 536 h using around 3 kWh of electricity per kg of CO<sub>2</sub>. By leveraging highly efficient and stable Bi-based catalysts and the solid electrolyte cell, the captured CO<sub>2</sub> was further converted into pure formic acid, achieving the stable production of 20.16 l of 0.45 M formic acid solution over 20 days. The pure formic acid solution served as a carbon substrate for microbial fermentation by a marine bacterium, resulting in the production of 1.13 g l<sup>-1</sup> succinic acid, a precursor for biodegradable plastics. The fermentation process was successfully scaled up, with sustained yields of 1.16 and 1.37 g l<sup>-1</sup> succinate in 1- and 5-l fermenters, respectively, exemplifying the practical potential of this system. As a proof of concept, we further produced high-quality PBS plastics using the as-obtained bio-derived succinate. Our system, therefore, offers a sustainable approach for the upcycling of CO<sub>2</sub> from the ocean and opens avenues for electrochemically driven biochemical synthesis.

#### **Methods**

#### Chemicals

Natural seawater was collected from Shenzhen Bay, China. EA ( $C_{14}H_6O_8$ , AR, 98%), bismuth nitrate (Bi( $NO_3$ ) $_3$ · $5H_2O$ , AR, 99%), potassium hydroxide (KOH, Ar, 95%), decahydronaphthalene ( $C_{10}H_{18}$ , Ar), *N*-methylpyrrolidone (NMP, AR, 99%), ethanol ( $C_2H_6O$ , AR, 99%), tin(II) chloride (SnCl $_2$ , Ar) and isopropanol (IPA, AR, 99.5%) were purchased from Macklin. Potassium bicarbonate (KHCO $_3$ , AR, 99.5%), 5% Nafion 117 solution, 1,4-butanediol (BDO, AR), trichloromethane (CHCl $_3$ , AR) and methanol (CH $_3$ OH, Ar) were purchased from Aladdin. All chemicals were used without further purification.

#### Synthesis of the catalyst

EA (80 mg, ~0.265 mmol), Bi(NO<sub>3</sub>)<sub>3</sub>·5H<sub>2</sub>O (257 mg, 0.53 mmol) and NMP (10 ml) were placed in a 20-ml pressure-resistant glass tube. The mixture was ultrasonically dissolved at room temperature for 30 min (note that EA did not completely dissolve at room temperature (RT)). The suspension (in the tube) was placed in a baking oven and incubated by progressive heating and cooling processes. The heating procedure was as follows: RT  $\rightarrow$  70 °C (1,800 min), 70 °C (for 1,000 min) and 70 °C  $\rightarrow$  RT (1,600 min). A regular single crystal was formed, as revealed by microscopic examination. A large gram-scale reaction was performed at the same concentration in a larger glass tube.

#### Synthesis of PBS

PBS was synthesized through a condensation reaction between succinic acid and BDO, the former obtained from our electro-biosynthesis system. The synthetic procedure can be divided into two steps: esterification of succinic acid and BDO to produce PBS oligomers, followed by polycondensation of the oligomers. Initially, 0.01 mol succinic acid, 0.01 mol BDO and 6 ml decahydronaphthalene were added to a three-necked flask. Subsequently,  $SnCl_2$  was added as catalyst in a molar ratio of 1:600 to the reactants, followed by heating under magnetic agitation to 150 °C under an Ar atmosphere. After distillation of the water, the temperature was raised to 200 °C under vacuum and maintained for a continuous reaction period of 10 h before being cooled to RT. CHCl $_3$  was subsequently added for dissolution, followed by filtration and precipitation with methanol to obtain white fibrous solid products. The PBS obtained was then dried at 50 °C for 24 h.

#### **Characterization techniques**

SCXRD was performed on a Bruker D8 Venture diffractometer with graphite-monochromated Mo K $\alpha$  radiation ( $\lambda = 0.71073$  Å). The crystal was kept at 173 K during data collection. The APEX3 program was used for data collection and reduction. The structures were solved with intrinsic phasing in the SHELXT program and refined by full-matrix least-squares fitting on  $F^2$  using the OLEX2 software with SHELXT. PXRD was performed on a Philips X'Pert Pro Super diffractometer with Cu K $\alpha$  radiation ( $\lambda = 1.54178 \text{ Å}$ ). The morphologies of the samples were observed by SEM (Zersss Supra 40), and TEM and STEM-EDS elemental mapping were conducted on a Tecnai G2 F20 S-TWIN instrument. XPS was conducted on a VG ESCALAB MK II instrument using Al Kα (1,486.6 eV) as the excitation source. The peak at 284.6 eV for C 1s was used as a reference for the binding energies, MALDI-TOF MS was performed on a Bruker Ultraflextreme spectrometer (355 nm Nd:YAG laser, 2,000 Hz). In situ XAFS spectra of the Bi L<sub>3</sub>-edge were recorded at a constant current of 200 mA at the BL11B beamline of the Shanghai Synchrotron Radiation Facility. The spectra were recorded in fluorescence mode with a Lytle detector in an H-cell, operated at 3.5 GeV in top-up mode. Demeter software was used to process the XAFS data. In situ Raman analysis was conducted using a LabRAM HR laser Raman analyser (Horiba/Jobin Yvon) equipped with a frequency-doubled Nd:YAG 785 nm laser. In situ electrochemical ATR-SEIRAS experiments were conducted on a Thermo Scientific Nicolet iS50 Fourier transform infrared (FTIR) spectrometer with silicon as the prismatic window at RT. Gel permeation chromatography was performed on an Agilent 1260 instrument equipped with a PLgel MIXED-B LS 300 × 7.5 mm column and differential refractive index detector.

#### **Electrochemical measurements**

The CO<sub>2</sub>RR was analysed under ambient conditions using a BioLogic VMP3 or CHI 1140 device. A conventional flow cell was used for typical three-electrode cell measurements. An Ag/AgCl wire immersed in a saturated KCl solution was used as the reference electrode, while the counter electrode on which the OER took place consisted of Ni foam or IrO<sub>x</sub>/Ti mesh. The working electrode was prepared by spraying a precursor ink (containing 18 mg catalyst mixed with 36 μl of 5% Nafion 117 solution dissolved in 5 ml IPA) uniformly onto a GDL (YLS-30T) with a mass loading of around 1 mg cm<sup>-2</sup>. All potentials measured against Ag/ AgCl were converted to the RHE scale using the relationship  $E_{RHE} = E_{Ag/}$  $_{\rm AgCl}$  + 0.197 + pH × 0.059, compensating for the solution resistance by 100%. For the conventional flow cell test, the working and counter electrodes were positioned on opposite sides of two 1-cm-thick polytetrafluoroethylene (PTFE) sheets, each containing channels measuring 0.5 cm × 1.5 cm, ensuring that the catalyst layer was in contact with the flowing electrolyte. The geometric surface area of the catalyst was measured as 0.75 cm<sup>2</sup>. A Nafion 117 membrane was sandwiched between the two PTFE sheets to separate the chambers. CO<sub>2</sub> flowed through the gas chamber behind the cathode, and the flow rate was monitored by an Alicat Scientific mass flow controller. The cathode chamber was supplied with 0.5 M KHCO<sub>3</sub> electrolyte at a constant flow rate of 1.8 ml min<sup>-1</sup>, while the anodic electrolyte consisted of 4 M KOH and was circulated around the anode at a rate of 25 ml min<sup>-1</sup>.

For the solid electrolyte cell to produce a pure solution of HCOOH, an AEM (Dioxide Materials or FuMA-tech) and Nafion-117 film were used for anion and cation exchange, respectively. The cathode consisted of a YLS-30T GDL electrode loaded with Bi-BEN at a density of around 1 mg cm $^{-2}$  (electrode area of 4 or 25 cm $^2$ ), while the anode was composed of titanium mesh loaded with  $\rm IrO_{x^*}$ . A porous sulfonated styrene-divinylbenzene co-polymer was used as the solid ion conductor (Amberchrom 50WX8, Sigma-Aldrich). An aqueous solution of 0.5 M  $\rm H_2SO_4$  was circulated around the anode side at a flow rate of 25 ml min $^{-1}$ . The HCOOH produced within the solid-state electrolyte layer was released using deionized water at a flow rate of 1.8 or 0.7 ml min $^{-1}$ . In the solid electrolyte cell test, none of the potentials measured using

the two-electrode set-up were compensated. Measurements were taken repeatedly from different samples, with each measurement conducted independently.

#### **Product analysis**

Gaseous products were analysed by online GC using a PerkinElmer Clarus 690 device equipped with a flame ionization detector, a thermal conductivity detector and a 5-Å molecular sieve column. Liquid products were quantified by ion chromatography (Thermo Fisher ICS-600) or 400 MHz NMR spectroscopy (Bruker). Typically, after electrolysis, 600  $\mu$ l electrolyte was mixed with 100  $\mu$ l D $_2$ O (Sigma Aldrich, 99.9 at% D) and 0.05  $\mu$ l dimethylsulfoxide (Sigma Aldrich, 99.9%) as internal standard. The pre-saturation method was used to suppress the water peak.

#### In situ DEMS measurements

In situ DEMS was performed using a custom-made electrochemical capillary DEMS flow cell. The catalysts were loaded onto the GDL as the cathode, behind which the  $\mathrm{CO}_2$  flowed. A capillary was placed in the gas outlet of the flow cell to draw the gas products into the DEMS sensor (PrismaPro). The signals at m/z=2 and 28 represent the products  $\mathrm{H}_2$  and  $\mathrm{CO}$ , respectively. The onset potentials were determined according to the positions at which the signal-to-noise ratios were greater than 5.

#### In situ ATR-SEIRAS measurements

In situ ATR-SEIRAS spectra were collected with an FTIR spectrometer (Thermo Scientific Nicolet iS50) equipped with an MCT-A detector. The catalyst inks were prepared by mixing 10 mg electrocatalyst, 5 ml ethanol and 25  $\mu$ l Nafion 117 solution. Then, 10  $\mu$ l ink solution was dropped onto the central area (confined by an O ring with a diameter of 8 mm) of an Au film deposited on the basal plane of a hemicylindrical Si prism by evaporation. The Si prism was assembled in a spectroelectrochemical cell with Pt wire as the counter electrode, Ag/AgCl wire in saturated KCl solution as the reference electrode and 0.5 M KHCO $_3$  solution pre-saturated and continuously bubbled with CO $_2$  as the electrolyte. All spectra were collected at a resolution of 4 cm $^{-1}$ , and each single-beam spectrum was an average of 200 scans. A CHI 1140 electrochemistry workstation (Shanghai CH Instruments) was used for potential control.

#### In situ Raman spectroscopy measurements

In situ Raman spectroscopy was carried out with a LabRAM HR laser Raman spectrometer (Horiba/Jobin Yvon) equipped with a frequency-doubled Nd:YAG (785 nm) laser. The catalyst inks were prepared by mixing 10 mg electrocatalyst, 2 ml IPA and 20  $\mu$ l Nafion 117 solution. The ink solution was sprayed onto carbon paper, and the carbon paper was assembled in a spectroelectrochemical cell with Pt wire as the counter electrode with Ag/AgCl wire in saturated KCl solution as the reference electrode and 0.5 M KHCO $_{\!3}$  solution as the electrolyte. During measurement, the laser was focused on the surface of the sample. A CHI 1140 electrochemistry workstation (Shanghai CH Instruments) was used for potential control.

#### Bacterial culture media

Two types of culture medium were used in this study, namely LBV2 and M9. The LBV2 medium contained (per litre) 20 g Luria–Bertani (LB) powder, 11.9 g NaCl, 0.313 g KCl and 2.2 g MgCl<sub>2</sub> with the ampicillin 100 mg ml<sup>-1</sup>. All solidified media for bacterial growth contained 1.5% (w/v) agar. The M9 medium contained (per litre) 1 g NH<sub>4</sub>Cl, 20 g NaCl, 6.78 g Na<sub>2</sub>HPO<sub>4</sub>, 3 g KH<sub>2</sub>PO<sub>4</sub>, 2 mM MgSO<sub>4</sub>, 0.1 mM CaCl<sub>2</sub> and 441 mM HCOOH, and the pH was adjusted to 7.5 before use.

#### **Plasmid construction**

The DNA fragments of the formate-THF ligase (*ftl*), methenyl-THF cyclohydrolase (*fch*) and methylene-THF dehydrogenase (*mtd*) genes were obtained from *M. extorquens*. The synthesized DNA fragment

was cloned and inserted into the plasmid vector pTrc99A-Amp and used to construct the plasmid pXG251. pXG251 was introduced into *V. natriegens* (ATCC 14048) with formic acid as the carbon source to construct strain XG251. pJ23119 (5′-3′:TTGACAGCTAGCTCAGTCCTAGGTATAATGCTAGCTCTAGAGATTAAAGAGGAGAAATACTAG) was used as the promoter. The DNA fragment *ftl-fch-mtd* was amplified using the primers ftl-fch-mtd-overlap-F (5′-3′:CATGTTCTTTTCCTGAAGTTTGA-CAGCTAGCTCAGTCCTAGGTATAATG) and ftl-fch-mtd-overlap-R (5′-3′:GTTATTGCTCAGCGGTGTTAGGCCATTTCCTTGGCCAG). The pTrc99A vector was amplified using the primers pTrc99A-overlap-F (5′-3′:CACCGCTGAGCAATAACTAGC) and pTrc99A-overlap-R (5′-3′:ACTTCAGGAAAGAACATGTGAGCAAAAG). The two fragments were assembled by Gibson assembly, resulting in the plasmid pTrc99A-*ftl-fch-mtd*. The plasmid pTrc99A-*ftl-fch-mtd* was introduced into the formic acid-utilizing *V. natriegens* XG251 to generate strain XG251.

#### Succinate fermentation

Initially, 2 ml LBV2 medium was inoculated with *V. natriegens* from glycerol stock and cultured at 37 °C for 6–8 h overnight. The following day, the cells were cultured with LBV2 medium containing 441 mM HCOOH until they reached OD  $_{600}$  = 1–1.5. The cells were collected at 4,000 g (centrifugation force) for 5 minutes at OD  $_{600}$  = 10, washed once with M9 medium and then 10 ml of the cell suspension was transferred to a 50-ml baffled flask for fermentation. Samples were removed at different time points for NMR analysis to determine the yield of succinate and the residual amount of formate.

#### Scaled-up production of succinate

The production of succinic acid from formic acid as the only carbon source was scaled up using the same bacterial cell collection process as described above. Fermentation was performed using 200 ml bacterial culture in a 1-l fermenter (DASbox Mini Bioreactor System, Eppendorf) and 1 bacterial culture in a 5-l fermenter (Biostat A, Sartorius Stedim Biotech). The fermentation tank was operated at a temperature of 37 °C and an agitation speed of 200 rpm. Samples were collected at specific time intervals to quantify succinate and formate. The production medium consisted of 6.78 g l $^{-1}$ Na $_2$ HPO $_4$  and 3 g l $^{-1}$ KH $_2$ PO $_4$ . During fermentation, the pH of the fermentation broth was controlled between 7.0 and 8.0 using 1 mol l $^{-1}$ KOH and 1 mol l $^{-1}$ HCl.

# Quantification of succinate production and the remaining HCOOH

The yield of succinate and residual formic acid in the test solutions were quantified by NMR spectroscopy using either an AVANCE NEO 400 or AVANCE III HD50 Bruker spectrometer. The test solutions consisted of 450  $\mu$ l of the sample solution and 50  $\mu$ l D<sub>2</sub>O. The collected data were processed and integrated using Bruker TopSpin software.

#### <sup>13</sup>C isotopomer analysis

*V. natriegens* cells were cultured in M9 medium (441 mM H<sup>12</sup>COOH) at 37 °C. After three generations, the cells were collected at an OD<sub>600</sub> of 2.0 using M9 medium (441 mM H<sup>13</sup>COOH). After 24 h, the culture medium was collected by centrifugation (16,099 g, 4 °C, 10 min) and 10  $\mu$ l of the culture supernatant was dried under N<sub>2</sub>. Subsequently, 80  $\mu$ l pyridine and 20  $\mu$ l *N*-methyl-*N*-(*tert*-butyldimethylsilyl)trifluoroacetamide were used for derivatization at 85 °C for 1 h. After filtration (0.22  $\mu$ m pore size, Millipore), 1  $\mu$ l of the sample was injected into a GC–MS system equipped with a DB-5HT column (30 × 0.25 mm, 0.1  $\mu$ m). The system was operated in electron impact mode at 70 eV. Succinic acid and <sup>13</sup>C-labelled succinic acid were determined by matching the mass and retention time with a validated standard library.

#### **Reporting summary**

Further information on research design is available in the Nature Portfolio Reporting Summary linked to this article.

#### **Data availability**

The data supporting the findings of this study are available within the Article and its Supplementary Information. The atomic coordinates of the optimized computational models are also provided in Supplementary Data 1. Other data that support the findings of this study are available from the corresponding authors upon reasonable request. Source data are provided with this paper.

#### References

- Friedlingstein, P. et al. Global carbon budget 2022. Earth Syst. Sci. Data 14. 4811–4900 (2022).
- Gruber, N. et al. Trends and variability in the ocean carbon sink. Nat. Rev. Earth Environ. 4, 119–134 (2023).
- Gattuso, J. P. et al. Contrasting futures for ocean and society from different anthropogenic CO<sub>2</sub> emissions scenarios. Science 349, aac4722 (2015).
- 4. DeVries, T. The ocean carbon cycle. *Annu. Rev. Environ. Resour.* 47, 317–341 (2022).
- de Lannoy, C.-F. et al. Indirect ocean capture of atmospheric CO<sub>2</sub>: part I. Prototype of a negative emissions technology. *Int. J. Greenh. Gas Control* 70, 243–253 (2018).
- Rahimi, M., Khurram, A., Hatton, T. A. & Gallant, B. Electrochemical carbon capture processes for mitigation of CO<sub>2</sub> emissions. *Chem. Soc. Rev.* 51, 8676–8695 (2022).
- Yan, L., Bao, J., Shao, Y. & Wang, W. An electrochemical hydrogen-looping system for low-cost CO<sub>2</sub> capture from seawater. ACS Energy Lett. 7, 1947–1952 (2022).
- Krause-Jensen, D. & Duarte, C. M. Substantial role of macroalgae in marine carbon sequestration. Nat. Geosci. 9, 737–742 (2016).
- Cai, L., Li, H., Deng, J., Zhou, R. & Zeng, Q. Biological interactions with *Prochlorococcus*: implications for the marine carbon cycle. *Trends Microbiol.* 32, 280–291 (2023).
- 10. Zhang, C. et al. Eco-engineering approaches for ocean negative carbon emission. *Sci. Bull.* **67**, 2564–2573 (2022).
- Orr, J. C. et al. Anthropogenic ocean acidification over the twenty-first century and its impact on calcifying organisms. Nature 437, 681–686 (2005).
- Kwiatkowski, L. & Orr, J. C. Diverging seasonal extremes for ocean acidification during the twenty-first century. *Nat. Clim. Change* 8, 141–145 (2018).
- Taylor, L. L. et al. Enhanced weathering strategies for stabilizing climate and averting ocean acidification. *Nat. Clim. Change* 6, 402–406 (2016).
- Eisaman, M. D. Negative emissions technologies: the tradeoffs of air-capture economics. *Joule* 4, 516–520 (2020).
- Eisaman, M. D. et al. CO<sub>2</sub> extraction from seawater using bipolar membrane electrodialysis. *Energy Environ. Sci.* 5, 7346–7352 (2012).
- Digdaya, I. A. et al. A direct coupled electrochemical system for capture and conversion of CO<sub>2</sub> from oceanwater. Nat. Commun. 11, 4412 (2020).
- 17. Sharifian, R., Boer, L., Wagterveld, R. M. & Vermaas, D. A. Oceanic carbon capture through electrochemically induced in situ carbonate mineralization using bipolar membrane. *Chem. Eng. J.* **438**, 135326 (2022).
- Kim, S. et al. Asymmetric chloride-mediated electrochemical process for CO<sub>2</sub> removal from oceanwater. *Energy Environ. Sci.* 16, 2030–2044 (2023).
- Aleta, P., Refaie, A., Afshari, M., Hassan, A. & Rahimi, M. Direct ocean capture: the emergence of electrochemical processes for oceanic carbon removal. *Energy Environ. Sci.* 16, 4944–4967 (2023).
- 20. Xia, C. et al. Continuous production of pure liquid fuel solutions via electrocatalytic CO<sub>2</sub> reduction using solid-electrolyte devices. *Nat. Energy* **4**, 776–785 (2019).

- Zhu, P. et al. Continuous carbon capture in an electrochemical solid-electrolyte reactor. *Nature* 618, 959–966 (2023).
- Fang, W. et al. Durable CO<sub>2</sub> conversion in the proton-exchange membrane system. *Nature* 626, 86–91 (2024).
- Chen, C., Kotyk, J. F. K. & Sheehan, S. W. Progress toward commercial application of electrochemical carbon dioxide reduction. Chem 4, 2571–2586 (2018).
- Claassens, N. J., Cotton, C. A. R., Kopljar, D. & Bar-Even, A. Making quantitative sense of electromicrobial production. *Nat. Catal.* 2, 437–447 (2019).
- Tian, J. et al. Discovery and remodeling of Vibrio natriegens as a microbial platform for efficient formic acid biorefinery. Nat. Commun. 14, 7758 (2023).
- 26. Yang, S. et al. Halide-guided active site exposure in bismuth electrocatalysts for selective  $\rm CO_2$  conversion into formic acid. *Nat. Catal.* **6**, 796–806 (2023).
- 27. Zhang, M. et al. Engineering a conductive network of atomically thin bismuthene with rich defects enables  $\mathrm{CO}_2$  reduction to formate with industry-compatible current densities and stability. Energy Environ. Sci. **14**, 4998–5008 (2021).
- Zhu, J. et al. Surface passivation for highly active, selective, stable, and scalable CO<sub>2</sub> electroreduction. Nat. Commun. 14, 4670 (2023).
- Li, Y. et al. Enhancing local CO<sub>2</sub> adsorption by l-histidine incorporation for selective formate production over the wide potential window. *Angew. Chem. Int. Ed.* 62, e202313522 (2023).
- Deng, W., Zhang, P., Seger, B. & Gong, J. Unraveling the rate-limiting step of two-electron transfer electrochemical reduction of carbon dioxide. *Nat. Commun.* 13, 803 (2022).
- 31. Fletcher, S. Tafel slopes from first principles. *J. Solid State Electrochem* **13**, 537–549 (2009).
- 32. Limaye, A. M., Zeng, J. S., Willard, A. P. & Manthiram, K. Bayesian data analysis reveals no preference for cardinal Tafel slopes in CO<sub>2</sub> reduction electrocatalysis. *Nat. Commun.* **12**, 703 (2021).
- Zhang, H., Gao, J., Raciti, D. & Hall, A. S. Promoting Cu-catalysed CO<sub>2</sub> electroreduction to multicarbon products by tuning the activity of H<sub>2</sub>O. Nat. Catal. 6, 807–817 (2023).
- 34. Shi, Y. et al. Unveiling hydrocerussite as an electrochemically stable active phase for efficient carbon dioxide electroreduction to formate. *Nat. Commun.* **11**, 3415 (2020).
- 35. Yao, K. et al. Metal-organic framework derived dual-metal sites for electroreduction of carbon dioxide to HCOOH. *Appl. Catal. B* **311**, 121377 (2022).
- Liu, C. et al. In situ reconstruction of Cu–N coordinated MOFs to generate dispersive Cu/Cu<sub>2</sub>O nanoclusters for selective electroreduction of CO<sub>2</sub> to C<sub>2</sub>H<sub>4</sub>. ACS Catal. 12, 15230–15240 (2022).
- 37. Yuan, Y. et al. In situ structural reconstruction to generate the active sites for CO<sub>2</sub> electroreduction on bismuth ultrathin nanosheets. *Adv. Energy Mater.* **12**, 2200970 (2022).
- Weinstock, M. T., Hesek, E. D., Wilson, C. M. & Gibson, D. G. Vibrio natriegens as a fast-growing host for molecular biology. Nat. Methods 13, 849–851 (2016).
- Lee, H. H. et al. Functional genomics of the rapidly replicating bacterium Vibrio natriegens by CRISPRi. Nat. Microbiol. 4, 1105–1113 (2019).
- Bang, J. & Lee, S. Y. Assimilation of formic acid and CO<sub>2</sub> by engineered *Escherichia coli* equipped with reconstructed one-carbon assimilation pathways. *Proc. Natl Acad. Sci. USA* 115, 9271–9279 (2018).
- Yishai, O., Goldbach, L., Tenenboim, H., Lindner, S. N. & Bar-Even, A. Engineered assimilation of exogenous and endogenous formate in *Escherichia coli*. ACS Synth. Biol. 6, 1722–1731 (2017).
- Ferone, M., Raganati, F., Olivieri, G. & Marzocchella, A. Bioreactors for succinic acid production processes. Crit. Rev. Biotechnol. 39, 571–586 (2019).

- 43. Nelson, T. F. et al. Biodegradation of poly(butylene succinate) in soil laboratory incubations assessed by stable carbon isotope labelling. *Nat. Commun.* **13**, 5691 (2022).
- 44. Dalia, T. N. et al. Multiplex genome editing by natural transformation (MuGENT) for synthetic biology in *Vibrio natriegens*. ACS Synth. Biol. **6**, 1650–1655 (2017).
- 45. Hoffart, E. et al. High substrate uptake rates empower *Vibrio natriegens* as production host for industrial biotechnology. *Appl. Environ. Microbiol.* **83**, e01614–e01617 (2017).
- Zhu, L. W. & Tang, Y. J. Current advances of succinate biosynthesis in metabolically engineered *Escherichia coli*. *Biotechnol*. *Adv.* 35, 1040–1048 (2017).
- 47. Xia, C., Xia, Y., Zhu, P., Fan, L. & Wang, H. Direct electrosynthesis of pure aqueous H<sub>2</sub>O<sub>2</sub> solutions up to 20% by weight using a solid electrolyte. *Science* **366**, 226–231 (2019).
- Xianbiao, F. et al. Scalable chemical interface confinement reduction BiOBr to bismuth porous nanosheets for electroreduction of carbon dioxide to liquid fuel. Adv. Funct. Mater. 32, 2107182 (2022).
- 49. Chen, L. -W. et al. Controllable crystallization of two-dimensional Bi nanocrystals with morphology-boosted CO₂ electroreduction in wide pH environments. Small 19, 2301639 (2023).
- Yang, Q. et al. Novel Bi-doped amorphous SnO<sub>x</sub> nanoshells for efficient electrochemical CO<sub>2</sub> reduction into formate at low overpotentials. Adv. Mater. 32, 2002822 (2020).
- 51. He, Y.-C. et al. Integrated 3D open network of interconnected bismuthene arrays for energy-efficient and electrosynthesis-assisted electrocatalytic CO<sub>2</sub> reduction. Small **18**, 2105246 (2022).
- Ma, W. Monoclinic scheelite bismuth vanadate derived bismuthene nanosheets with rapid kinetics for electrochemically reducing carbon dioxide to formate. Adv. Funct. Mater. 31, 2006704 (2021).
- 53. Xing, Y. et al. Bi@Sn core-shell structure with compressive strain boosts the electroreduction of  $CO_2$  into formic acid. *Adv. Sci.* **7**, 1902989 (2020).
- 54. Lv, L. e al. Coordinating the edge defects of bismuth with sulfur for enhanced  $CO_2$  electroreduction to formate. *Angew. Chem. Int. Ed.* **62**, e202303117 (2023).
- Chen, L., Liu, Y., Kong, X., Geng, Z. & Zeng, J. Electrodeposited highly-oriented bismuth microparticles for efficient CO<sub>2</sub> electroreduction into formate. *Nano Res.* 15, 10078–10083 (2022).
- Zeng, G. et al. Reconstruction of ultrahigh-aspect-ratio crystalline bismuth-organic hybrid nanobelts for selective electrocatalytic CO<sub>2</sub> reduction to formate. Adv. Funct. Mater. 32, 2201125 (2022).
- 57. Zhao, Y. et al. Spontaneously Sn-doped  $Bi/BiO_x$  core-shell nanowires toward high-performance  $CO_2$  electroreduction to liquid fuel. *Nano Lett.* **21**, 6907–6913 (2021).
- Nguyen, D. T. N. et al. Metabolic engineering of the type I methanotroph Methylomonas sp. DH-1 for production of succinate from methane. *Metab. Eng.* 54, 170–179 (2019).
- Mock, M., Schmid, A. & Bühler, K. Directed reaction engineering boosts succinate formation of Synechocystis sp. PCC 6803\_Δ sll1625. Biotechnol. J. 15, 2000127 (2020).

#### **Acknowledgements**

C.X. acknowledges the National Key Research and Development Program of China (2024YFB4105700), the NSFC (52171201) and the Natural Science Foundation of Sichuan Province (2025NSFJQ0017). X.G. acknowledges the NSFC (32230060, 32171426, 32522056), the Guangdong Basic and Applied Basic Research Foundation (2024B1515020102) and the Shenzhen Science and Technology Program (JCYJ20220818101804010, JCYJ20220531100006011 and RCYX20221008092901004). We thank beamline BL11B of the Shanghai Synchrotron Radiation Facility and Shenzhen Synthetic Biology Infrastructure for providing facilities. We extend our gratitude to W. Jiang and Y. Gu's group for their generous provision of the starting *V. natriegens* strains.

#### **Author contributions**

The project was conceptualized by C.X. and was supervised by C.X. and X.G. C. Li prepared the catalysts with the help of B.Y. C. Li performed the catalytic tests. M.G., S.P. and M.H. performed the microbial experiments. C. Li, B.Y., H.Z. and Y.J. performed the catalyst characterization. C. Li, X.L., Q.J. and T.Z. designed the membrane electrode. C. Li, C. Liu and W.X. performed the XAFS measurements. C. Li, M.G., H.W., J.L., X.Z., Y.W., D.Z. and K.Z. helped in the data analysis. J.Z. and L.Z. performed the DFT calculations. C.X., C. Li, M.G. and X.G. wrote the paper with input from all of the authors. All of the authors discussed the results and commented on the paper.

#### **Competing interests**

A provisional patent application (202310817899.5) based on the technology described in this work was filed in China on July 2023 by C.X. and C. Li. at the University of Electronic Science and Technology of China. The other authors declare no other competing interests.

#### **Additional information**

**Supplementary information** The online version contains supplementary material available at https://doi.org/10.1038/s41929-025-01416-4.

**Correspondence and requests for materials** should be addressed to Xiang Gao or Chuan Xia.

**Peer review information** *Nature Catalysis* thanks Asmita Jana and the other, anonymous, reviewer(s) for their contribution to the peer review of this work

**Reprints and permissions information** is available at www.nature.com/reprints.

**Publisher's note** Springer Nature remains neutral with regard to jurisdictional claims in published maps and institutional affiliations.

Springer Nature or its licensor (e.g. a society or other partner) holds exclusive rights to this article under a publishing agreement with the author(s) or other rightsholder(s); author self-archiving of the accepted manuscript version of this article is solely governed by the terms of such publishing agreement and applicable law.

© The Author(s), under exclusive licence to Springer Nature Limited 2025

# nature portfolio

| Corresponding author(s):   | Chuan Xia, Xiang Gao |
|----------------------------|----------------------|
| Last updated by author(s): | Jul 18, 2025         |

# **Reporting Summary**

Nature Portfolio wishes to improve the reproducibility of the work that we publish. This form provides structure for consistency and transparency in reporting. For further information on Nature Portfolio policies, see our <u>Editorial Policies</u> and the <u>Editorial Policy Checklist</u>.

| _ |   |    |     | _     |
|---|---|----|-----|-------|
| C | - | +: | ςt  | : ~ ~ |
|   | и | 11 | ST. | ורכ   |

| For         | all statistical analyses, confirm that the following items are present in the figure legend, table legend, main text, or Methods section.  |
|-------------|--|
| n/a         | Confirmed  |
|             | $\square$ The exact sample size (n) for each experimental group/condition, given as a discrete number and unit of measurement  |
|             | 🔀 A statement on whether measurements were taken from distinct samples or whether the same sample was measured repeatedly  |
| $\boxtimes$ | The statistical test(s) used AND whether they are one- or two-sided  Only common tests should be described solely by name; describe more complex techniques in the Methods section.  |
| $\boxtimes$ | A description of all covariates tested   |
| $\boxtimes$ | A description of any assumptions or corrections, such as tests of normality and adjustment for multiple comparisons  |
|             | A full description of the statistical parameters including central tendency (e.g. means) or other basic estimates (e.g. regression coefficient) AND variation (e.g. standard deviation) or associated estimates of uncertainty (e.g. confidence intervals) |
| $\boxtimes$ | For null hypothesis testing, the test statistic (e.g. <i>F</i> , <i>t</i> , <i>r</i> ) with confidence intervals, effect sizes, degrees of freedom and <i>P</i> value noted <i>Give P values as exact values whenever suitable.</i>                        |
| $\boxtimes$ | For Bayesian analysis, information on the choice of priors and Markov chain Monte Carlo settings   |
| $\boxtimes$ | For hierarchical and complex designs, identification of the appropriate level for tests and full reporting of outcomes   |
| $\boxtimes$ | Estimates of effect sizes (e.g. Cohen's <i>d</i> , Pearson's <i>r</i> ), indicating how they were calculated   |
|             | Our web collection on <u>statistics for biologists</u> contains articles on many of the points above.  |

#### Software and code

Policy information about availability of computer code

Data collection

Provide a description of all commercial, open source and custom code used to collect the data in this study, specifying the version used OR state that no software was used.

Data analysis

Provide a description of all commercial, open source and custom code used to analyse the data in this study, specifying the version used OR state that no software was used.

For manuscripts utilizing custom algorithms or software that are central to the research but not yet described in published literature, software must be made available to editors and reviewers. We strongly encourage code deposition in a community repository (e.g. GitHub). See the Nature Portfolio guidelines for submitting code & software for further information.

#### Data

Policy information about availability of data

All manuscripts must include a <u>data availability statement</u>. This statement should provide the following information, where applicable:

- Accession codes, unique identifiers, or web links for publicly available datasets
- A description of any restrictions on data availability
- For clinical datasets or third party data, please ensure that the statement adheres to our policy

The data supporting the findings of this study are available within the Article and its Supplementary Information. Source data are provided with this paper. The

| atomic coordinates of the optim<br>corresponding authors upon rea | nized computational models are also provided. Other data that support the findings of this study are available from the asonable request.                    |  |  |
|---|--|--|--|
|   | ·  |  |  |
| Research involving  | human participants, their data, or biological material   |  |  |
| Policy information about stud<br>and sexual orientation and ra    | dies with <u>human participants or human data</u> . See also policy information about <u>sex, gender (identity/presentation),</u> ace, ethnicity and racism. |  |  |
| Reporting on sex and gend   | er N/A   |  |  |
| Reporting on race, ethnicit other socially relevant groupings     | y, or N/A  |  |  |
| Population characteristics  | N/A  |  |  |
| Recruitment   | N/A  |  |  |
| Ethics oversight  | N/A  |  |  |
| Note that full information on the                                 | e approval of the study protocol must also be provided in the manuscript.  |  |  |
|   |  |  |  |
| Field-specific  | reporting  |  |  |
| Please select the one below t                                     | that is the best fit for your research. If you are not sure, read the appropriate sections before making your selection.                                     |  |  |
| X Life sciences   | Behavioural & social sciences Ecological, evolutionary & environmental sciences  |  |  |
|   | nt with all sections, see <u>nature.com/documents/nr-reporting-summary-flat.pdf</u>  |  |  |
| Life sciences   | study design   |  |  |
|   | these points even when the disclosure is negative.   |  |  |
| Sample size Sample si   | ze of three (n=3) or more was taken following previous papers in this field.   |  |  |
| Data exclusions No data w   | No data were excluded from the analyses.   |  |  |
| Replication At least th   | At least three independent and successful measurements were performed.   |  |  |
| Randomization Experime  |  |  |  |
|   | Investigators performing the experiment were blinded to data collection. The researchers performing analytics were blinded for strain information.           |  |  |
|   |  |  |  |
| Reporting for   | specific materials, systems and methods  |  |  |
| <u> </u>  | thors about some types of materials, experimental systems and methods used in many studies. Here, indicate whether each material,                            |  |  |
| system or method listed is releva                                 | ant to your study. If you are not sure if a list item applies to your research, read the appropriate section before selecting a response.                    |  |  |
| Materials & experimen   | tal systems Methods  |  |  |
| /a Involved in the study n/a Involved in the study                |  |  |  |
| Antibodies  | ChIP-seq   |  |  |
| Eukaryotic cell lines   | Flow cytometry   |  |  |
| Palaeontology and arc   | alaeontology and archaeology MRI-based neuroimaging  |  |  |
| Animals and other organisms                                       |  |  |  |
| Clinical data   |  |  |  |
| Dual use research of concern                                      |  |  |  |
|   |  |  |  |

## Plants

| Seed stocks           | N/A |
|-----------------------|-----|
|                       |     |
| Novel plant genotypes | N/A |
|                       |     |
|                       |     |
| Authentication        | N/A |
|                       |     |